Supporting Information

Monolayers of a Thiacalix[3]pyridine-Supported Molybdenum(0) Tricarbonyl Complex on Au(111): Characterisation with Surface Spectroscopy and Scanning Tunneling Microscopy

Kai Uwe Clausen[a], Xiangzhi Meng[b], Katrin Reisig[a], Christian Näther[a], Thomas Strunskus[c], Richard Berndt[b] and Felix Tuczek*[a]

[a] Institute of Inorganic Chemistry, Christian Albrechts University Kiel, Germany

[b] Institute of Experimental and Applied Physics, Christian Albrechts University Kiel, Germany

[c] Department of Material Science, Christian Albrechts University Kiel, Germany

Table of Contents

1 Instrumentation and Physical Methods

General Synthetic Procedures

Commercially available starting materials and solvents were used as received. Water and oxygen sensitive reagents were handled in a M. Braun Labmaster 130 Glovebox under nitrogen or argon atmosphere (H_2O < 1 ppm, O_2 < 1 ppm). Moisture and air sensitive reactions were carried out in dried solvents under N_2 atmosphere using standard Schlenk techniques (N_2 dried over P_4O_{10}). Toluene and *n*-pentane were dried over CaH_2 under Ar and were distilled prior to use.

Column Chromatography

Column chromatography was performed manually using silica gel 60 (0.04-0.063 mm) from Merck. An aquarium pump was used to generate a low external pressure. Rf-values were determined by thin-layer chromatography on Polygram Sil G/UV254 (Macherey-Nagel, 0.2 mm particle size) with a UV lamp (λ=254nm) by co. Camag.

IR and Raman Spectroscopy

Infrared spectra were recorded at room temperature on a Bruker Alpha FT-IR Spectrum with Platinum ATR setup or on a Bruker Vertex70 FT-IR spectrometer using a broadband spectral range extension VERTEX FM for full mid and far IR in the range of 6.000-80 cm^{-1}. Raman spectra were recorded at RT on a Bruker RAM II FT-Raman spectrometer using a liquid nitrogen cooled, highly sensitive Ge detector, 1064 nm radiation and 3 cm^{-1} resolution.

NMR Spectroscopy

NMR spectra were recorded with a Bruker AVANCE III HD Pulse Fourier Transform spectrometer equipped with a cryo-probehead Prodigy BBO400S1 BB-H&F-D-05-Z operating at frequencies of 400.13 MHz (^1H) and 100.62 MHz (^{13}C). Referencing was performed using the solvent residue signal (2.50 ppm for DMSO-d_6, 7.26 ppm for $CDCl_3$). Anhydrous deuterated solvents were freeze-pump-thaw degassed and dried over 3 Å molecular sieves.

Single Crystal X-Ray Structure Determination

Data collection was performed with a XtaLAB Synergy, Dualflex, HyPix diffractometer using CuKα radiation (λ = 1.54184). The structure was solved with SHELXT[1] and refined with SHELXL[2] using Least Squares minimisation. All non-hydrogen atoms were refined anisotropic. All non-hydrogen atoms were refined anisotropic. The C-H H atoms were positioned with idealized geometry (methyl H atoms allowed to rotate but not to tip) and were refined isotropic with $U_{iso}(H) = 1.2\ U_{eq}(C)$ (1.5 for methyl H atoms) using a riding model. The asymmetric unit contain half a molecule of dimethylsulfoxide as solvent that is located on a 2-fold screw axis. The S and C atoms of this DMSO molecules are disordered in two orientations and were refined using a split model with restraints. This disorder remain constant if the structure is refined in space group *C*2 or *Cc*.

A table with selected crystal data and results for the structure refinement can be found in **Table S1** and ORTEP plots are presented in **Figure S9**. CCDC-2366199 (**1**) contain the supplementary crystallographic data for this paper. These data can be obtained free charge from the Cambridge Crystallographic Data Centre via:

http://www.ccdc.cam.ac.uk/data_request/cif.

Elemental Analysis

The elemental analyses were performed using a Vario MICRO cube element analyzer by co. Elementar; the samples were prepared in tin vessels and were burnt in a stream of oxygen.

STM

The measurements were carried out with an ultrahigh vacuum cryogenic (~ 4.6 K) STM (Createc) with the base pressure better than 1.2×10^{-10} mbar. The Au(111) and Ag(111) surfaces were cleaned by repeated cycles of Ar+ sputtering (1.5 keV) and subsequent annealing to 773 K. $[Mo(CO)_3(Py_3S_3)]$ (**1**) was sublimated from a crucible at ≈ 420 K onto the metal surface held at room temperature at pressures $\leqslant 10^{-9}$ mbar. STM tips were prepared from W wire by electrochemical etching and subsequent annealing in vacuum followed by repeated indenting into the substrate.

Gold Substrate

Glass substrates with a 50 Å titanium adlayer and a 200 nm evaporated gold film from EMF corporation (Ithaca, NY) were used for IRRAS measurements. XPS and NEXAFS measurements were made with sputtered Au(111) single crystals. The gold wafer and single crystals were cleaned before each preparation by flame annealing in butane gas.

Preparation of Monolayers for IRRAS, XPS and NEXAFS measurements

Monolayers of $[Mo(CO)_3(Py_3S_3)]$ (**1**) were prepared by immersing Au(111) substrates (single crystals) in 0.5 mM solutions of the respective compound in dry acetone at room temperature under nitrogen or argon atmosphere. After 1 hours of immersion the sample was removed from the solution, rinsed with acetone and dried in a stream of nitrogen or argon gas.

IRRAS

The surface adsorbed molecules were investigated by using a Bruker VERTEX 70 FT-IR spectrometer equipped with a Polarization Modulation Accessory (PMA) 50 unit (Bruker Optik GmbH, Ettlingen, Germany). This instrument allows recording IRRAS and PM-IRRAS data with a spectral range from 4000 cm^{-1} down to 750 cm^{-1}. IRRAS data were collected with a liquid nitrogen cooled MCT detector in a horizontal reflection unit for grazing incidence (Bruker A518). The sample chamber was purged with dry nitrogen before and during measurements. A p-polarized beam at an incident angle of 80° to the surface normal was used for measurements. PM-IRRAS data were collected with the PMA 50 accessory using a liquid nitrogen-cooled MCT detector. The PEM maximum efficiency was set for the half-wave at 1750 cm^{-1} for analysis of the area from 2000 cm^{-1} to 1000 cm^{-1}. All spectra were recorded with 4 cm^{-1} resolution.
Air-sensitive samples were measured with a special designed inert-gas cell. In addition to an exposure window, this cell also has two hose connections to change the atmosphere.
Processing of PM-IRRAS data was carried out using the OPUS software Version 6.5 (Bruker, Germany). Baseline correction of the resulting IRRAS data was performed by the rubber band method in an interactive mode. PM-IRRAS data were processed by the implicit removal of the Bessel function through manual baseline correction.

XPS and NEXAFS

The XPS and NEXAFS measurements were performed at the BESSY II synchrotron radiation facility using the PREVAC endstation at the beamline HE-SGM. The experimental station is equipped with a hemispherical VG Scienta R3000 photoelectron analyzer. The energy resolution E/DE of the beamline with 150 mm slits is 800. XP survey spectra were secured at 700 eV photon energy using an analyzer pass energy of 100 eV, whereas for the C 1s, S 2p and Mo 3d spectra the photon energy used was 350 eV with pass energy of 50 eV. For N 1s spectra the photon energy was at 500 eV with pass energy of 50 eV. All spectra were acquired at normal electron emission. For determination of the relative composition of the molybdenum complex **1**, the XP spectra were energy-corrected using the Au $4f_{7/2}$ line at a binding energy of 84.0 eV as reference. Background correction was performed using a combination of a Shirley and a linear background for all signals. Peak fitting was performed using the program CASA XPS. The fitting parameter are shown in **Table S 3-S 4**.
The samples of $[Mo(CO)_3(Py_3S_3)]$ (**1**) were transported with a transfer-box from the nitrogen glovebox to the beamline, to protect the samples from contact with oxygen. To correct for the photon flux of the NEXAFS measurements, all spectra were divided by the spectrum obtained for a freshly sputtered clean gold substrate and then edge-step normalized (using the average intensities for the C K-edge between 275 ± 0.5 eV and 320 ± 0.5 eV and for the N K-edge between 395 ± 0.5 eV and 420 ± 0.5 eV as pre- and post-edge).

Powder Diffraction

THE XRPD pattern was measured with a STOE Stadi-P diffractometer equipped with a MYTHEN 1K detector (DECTRIS) using Cu-Kα1 radiation (λ = 1.5406 Å).

Computational Details

All computations were carried out using the ORCA 4.2.1 program package.[3] The properties of all studied structures were computed in the most stable spin state, which was determined through theoretical analysis. Geometry optimization and thermodynamic energy calculations were carried out with the PBE0 functional[4] and def2-TZVP[5,6] basis set. In addition, Grimme's dispersion correction[7] with Becke-Johnson damping (D3BJ) and the RIJCOSX density fitting approximation using the def2/J fitting basis set[8–11] were used for all calculations. Local minima were confirmed, when no imaginary frequency was found in the harmonic vibrational frequency calculations. With the optimized structures C 1s and N 1s core to valence electronic spectra were calculated. This was done in the framework of TDDFT with the hybrid DFA B3LYP,[12] the def2-TZVPP basis set,[5] the RIJCOSX approximation[8] and fine numerical integration grids (grid6 and gridX6 in ORCA nomenclature). The orbital window from which electrons were to be excited was restricted to the 1s orbital of the atom of interest. On this atom the integral accuracy was increased and 80 roots with electric quadrupole contributions computed. This was repeated for every unique C and N atom in the molecule. Local symmetry was exploited when appropriate so not every single atomic spectrum had to be calculated.

Single Point energies were determined with the PBE0 functional[4] and a def2-QZVPP[5] basis set. Solvation corrections were performed in THF solution using the solvation model based on density (SMD).[13] The solvation free energy Δ*G*solv was approximated using the gas-phase and solvated single-point energies (Δ*G*solv ≈ Esoln – Egas).[14] In addition, Grimme´s dispersion correction with Becke-Johnson damping (D3BJ) and the RIJCOSX density fitting approximation using the def2/J fitting basis set[8–11] were used.

2 Experimental Section

2.1 Synthesis of [Mo(CO)$_3$(Py$_3$S$_3$)] (1)

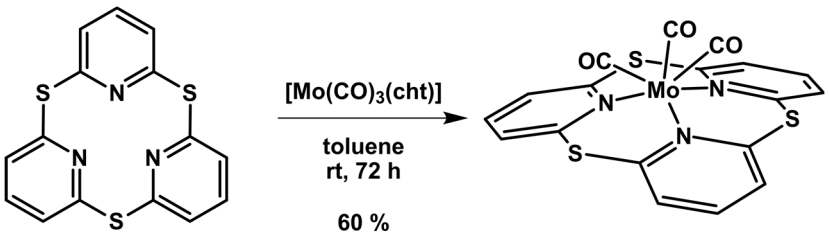

2 **1**

The synthesis was performed under nitrogen atmosphere. At first, the precursor cycloheptatrienemolybdenum(0) tricarbonyl [Mo(CO)$_3$(cht)] (239 mg, 878 µmol) was dissolved in toluene (5 mL). A solution of the ligand Py$_3$S$_3$ (**2**) (300 mg, 916 µmol) in toluene (35 mL) was added. Afterwards, the reaction mixture was stirred at rt for 72 h. The suspension was filtered and the precipitate was washed with toluene (10 mL) and *n*-pentane (2x 20 mL). After drying under vacuum the product was obtained as red powder (280 mg, 552 µmol, 60 %). Crystals for X-ray studies were grown by slow diffusion of diethylether in a solution of **2** in dimethyl sulfoxide (DMSO) at rt.

^{1}H NMR (400.1 MHz, DMSO-d$_6$): δ = 7.95 (m, 9H, py *H*^{3,4,5}) ppm.

^{13}C NMR (100.6 MHz, DMSO-d$_6$): δ = 232.7 (s, *C*O), 156.1 (s, py *C*^{2,6}), 138.7 (s, py *C*^{4}), 128.1 (s, py *C*^{3,5}) ppm.

IR (ATR): $\tilde{\nu}$ = 3102 (w), 3069 (w), 3059 (w), 3042 (w), 1888 (s), 1782 (s), 1761 (s), 1561 (m), 1540 (m), 1419 (m), 1385 (m), 1369 (m), 1257 (w), 1223 (w), 1174 (m), 1130 (m), 1091 (w), 1001 (w), 987 (w), 908 (w), 801 (m), 785 8m), 737 (m), 672 (w), 652 (w), 628 (m), 604 (m), 533 (m), 485 (w), 463 (w), 430 (w) cm^{-1}.

Raman: $\tilde{\nu}$ = 3101 (w), 3068 (w), 1888 (s), 1782 (m), 1761 (w), 1564 (s), 1419 (w), 1385 (m), 1371 (m), 1151 (w), 1007 (s), 798 (w), 731 (w), 679 (m), 629 (w), 536 (w), 503 (s), 463 8m), 430 (m), 405 (w), 266 (m), 220 (m), 189 (w), 166 (m), 129 (w), 112 (w) cm^{-1}.

HRMS (ESI): *m*/*z* calcd for $C_{18}H_9N_3S_3O_3Mo$: 508.8850 [M]$^+$; Found: 508.8855.

Anal. Calcd for $C_{18}H_9N_3S_3O_3Mo$:

	C %	H %	N %	S %
calculated	42.61	1.79	8.28	18.95
Found	42.51	2.05	8.36	18.91

2.2 Synthesis of Thiacalix[3](2,6)pyridine (2) (Py_3S_3)

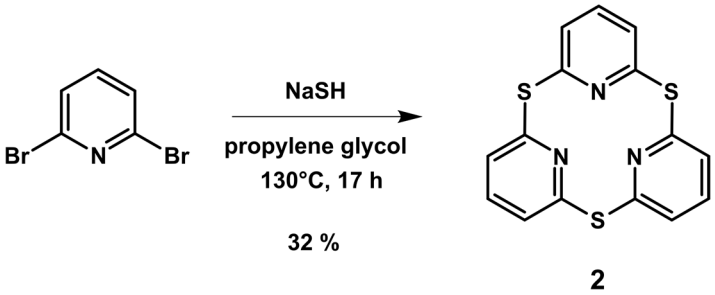

2

The synthesis was performed under nitrogen atmosphere. 2,6-Dibromopyridine (15.8 g, 66.6 mmol) and sodium hydrosulfide (NaSH x H_2O) (8.37 g, 149.3 mmol) was displaced in a schlenk flask and was dissolved in propylene glycol (100 mL). The reaction mixture was stirred for 17 h at 130°C. Afterwards, the solvent was removed by vacuum destillation (50°C, 0.1-0.07 mbar). The residue was dissolved in a mixture of dichloromethane (150 mL), sat. NaCl-solution (25 mL) and deion. Water (50 mL). The organic phase was separated and the aqueous phase was washed three times with dichloromethane (30 mL, each). The combined organic phase was dried over $MgSO_4$, filtrated, rinsed twice with dichloromethan (30 mL each) and the solvent was removed in vacuo. The product was purified by column chromatography (silica gel, dichloromethane). Final impurities were removed by dissolving the obtained solid in dichloromethane (10 mL) and precipitating by adding cyclohexane (250 mL), followed by filtration and drying in vacuo. The product was obtained as white solid in a yield of 2.30 g (7.02 mmol, 32 %).

R_f = 0.07 (dichloromethane), = 0.67 (dichloromethane / acetone 10:1)

^{1}H NMR (400.1 MHz, $CDCl_3$): δ = 7.49 (dd, ^{3}J = 8.1 Hz, 3J = 7.3 Hz, 3 H, py H^4), 7.30 (m, 6H, py $H^{3,5}$) ppm.

^{13}C NMR (100.6 MHz, $CDCl_3$): δ = 155.5 (s, py $C^{2,6}$), 137.3 (s, py C^4), 125.1 (s, py $C^{3,5}$) ppm.

IR (ATR): $\tilde{\nu}$ = 3066 (w), 3028 (w), 1555 (s), 1547 (s), 1416 (s), 1369 (m), 1243 (w), 1161 (m), 1147 (m), 1120 (s), 1078 (m), 979 (m), 909 (w), 894 (w), 796 (s), 782 (s), 728 (s), 653 (m), 619 (w), 598 (m), 563 (w), 534 (w), 492 (w), 481 (w), 424 (w) cm^{-1}.

Raman: $\tilde{\nu}$ = 3103 (w), 3078 (w), 3066 (m), 3055 (m), 3032 (w), 1552 (m), 1417 (w), 1390 (m), 1369 (w), 1243 (m), 1163 (m), 1147 (m), 1124 (m), 1078 (m), 989 (m), 982 (s), 889 (w), 795 (m), 786 (m), 777 (w), 652 (m), 451 (w), 395 8m), 289 (m), 210 (m), 162 (s), 147 (s) cm^{-1}.

HRMS (ESI): *m*/*z* calcd for $C_{15}H_{10}N_3S_3$: 328.0031 $[M-H]^+$; Found: 328.0028.

Anal. Calcd for $C_{15}H_9N_3S_3$:

	C %	H %	N %	S %
calculated	55.02	2.77	12.83	29.37
Found	55.11	3.06	12.54	29.59

2.3 NMR spectroscopy of [Mo(CO)$_3$(Py$_3$S$_3$)] (1)

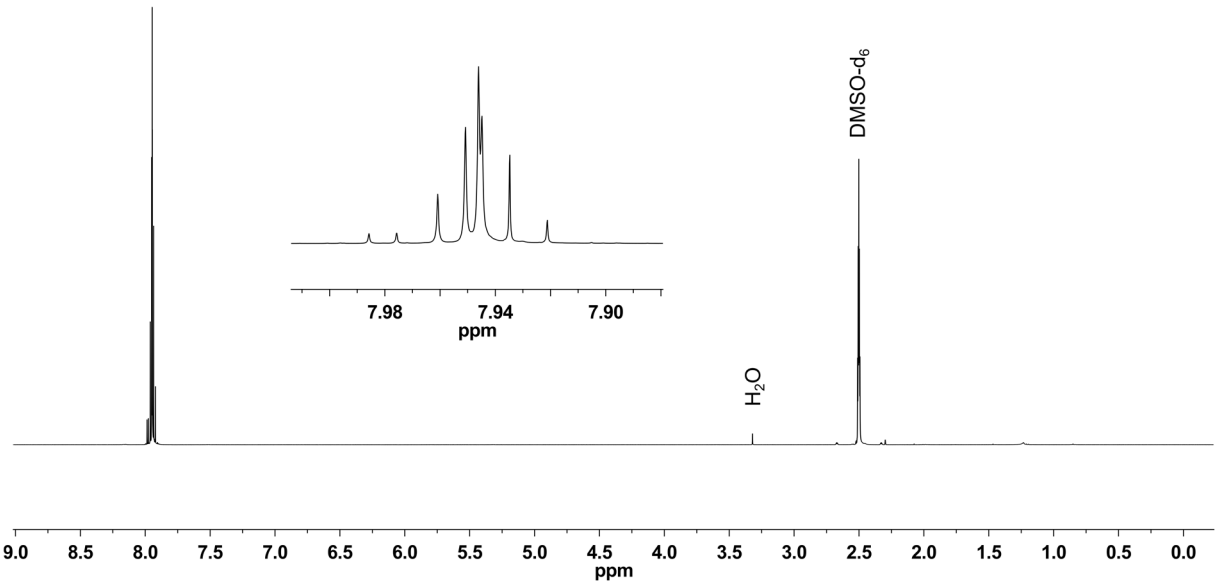

Figure S 1: ^{1}H NMR spectrum of [Mo(CO)$_3$(Py$_3$S$_3$)] (**1**) measured in DMSO-d$_6$ at 300 K.

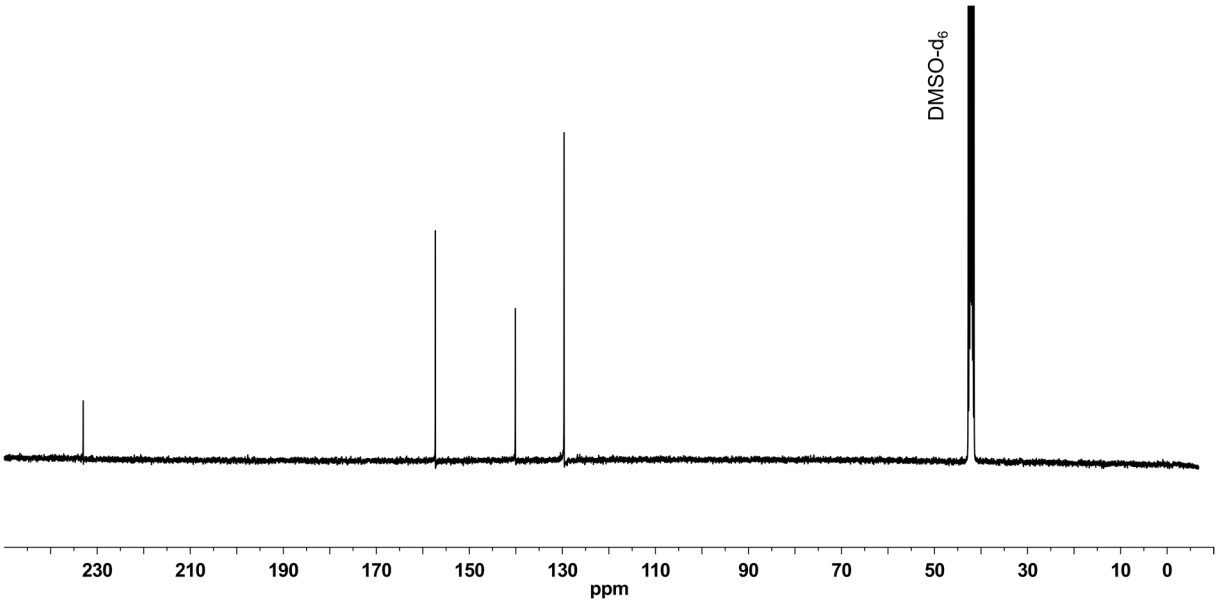

Figure S 2: ^{13}C NMR spectrum of [Mo(CO)$_3$(Py$_3$S$_3$)] (**1**) measured in DMSO-d$_6$ at 300 K.

2.4 NMR spectroscopy of Thiacalix[3](2,6)pyridine (Py_3S_3) (2)

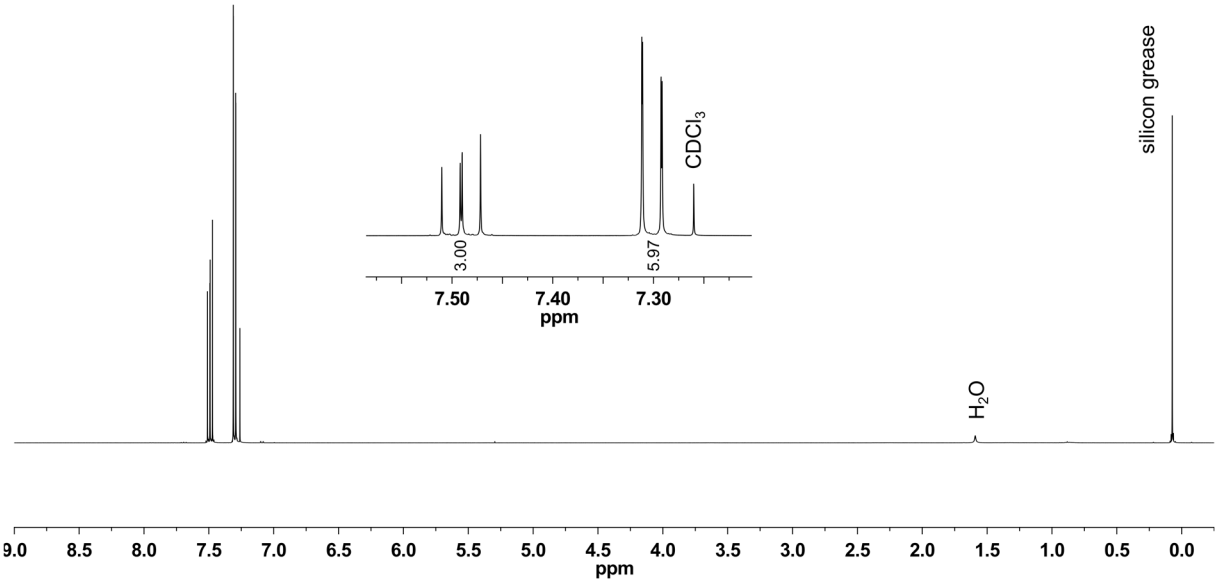

Figure S 3: ^{1}H NMR spectrum of Thiacalix[3](2,6)pyridine (Py_3S_3) (**2**) measured in $CDCl_3$ at 300 K.

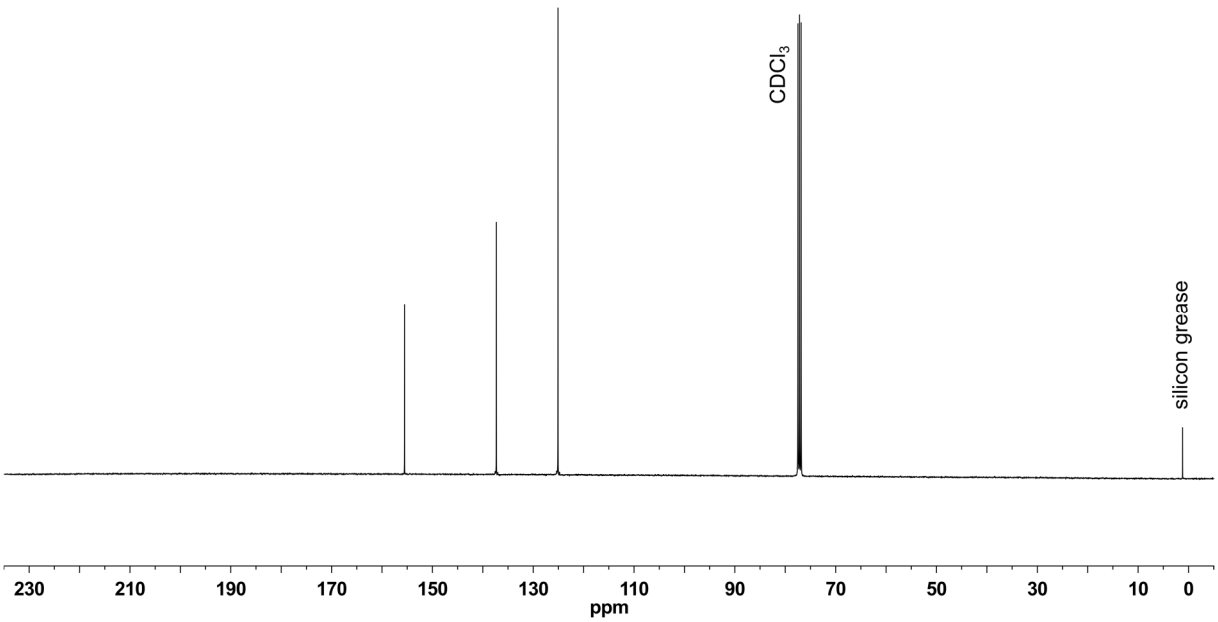

Figure S 4: ^{13}C NMR spectrum of Thiacalix[3](2,6)pyridine (Py_3S_3) (**2**) measured in $CDCl_3$ at 300 K.

2.5 Mass spectrometry of $[Mo(CO)_3(Py_3S_3)]$ (1)

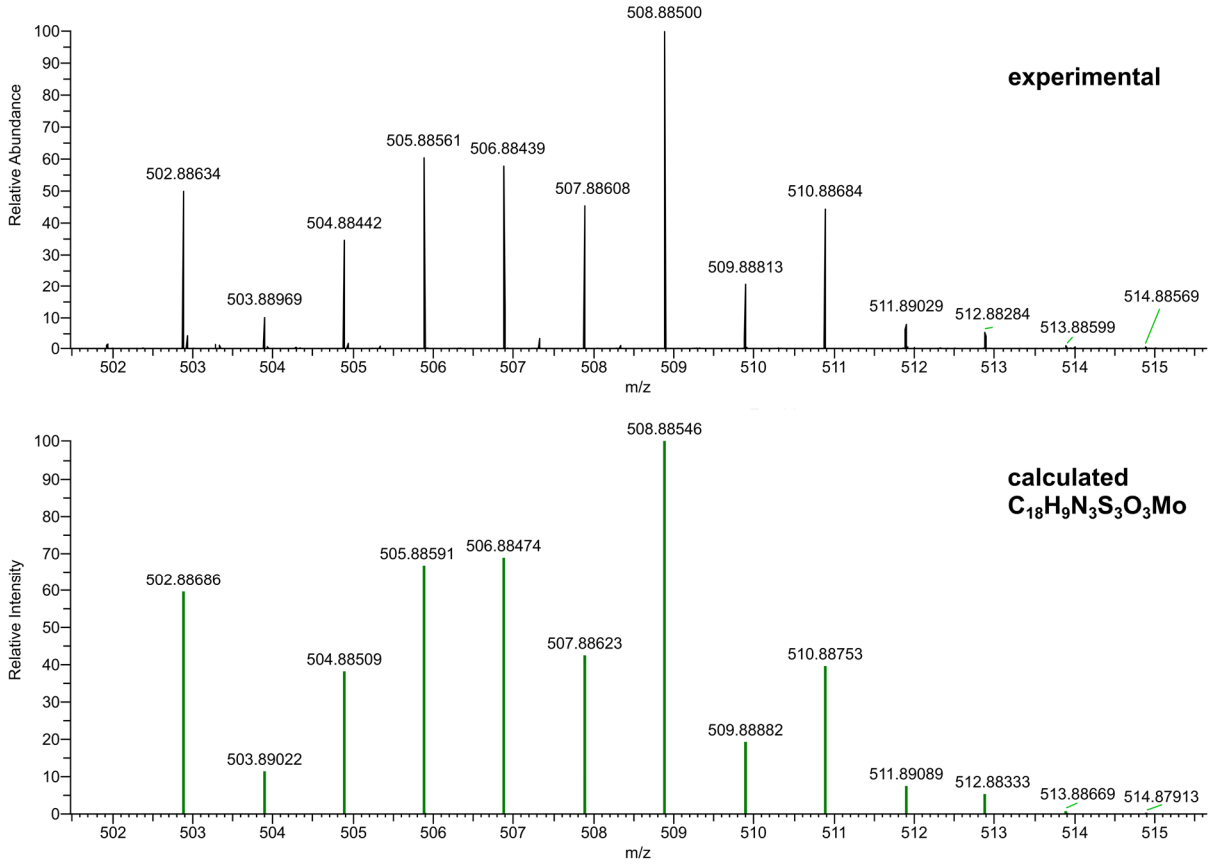

Figure S 5: Mass spectrum of $[Mo(CO)_3(Py_3S_3)]$ (**1**) with the isotopic pattern of the molecular peak $[M]^+$.

2.6 Mass spectrometry of Thiacalix[3](2,6)pyridine (Py_3S_3) (2)

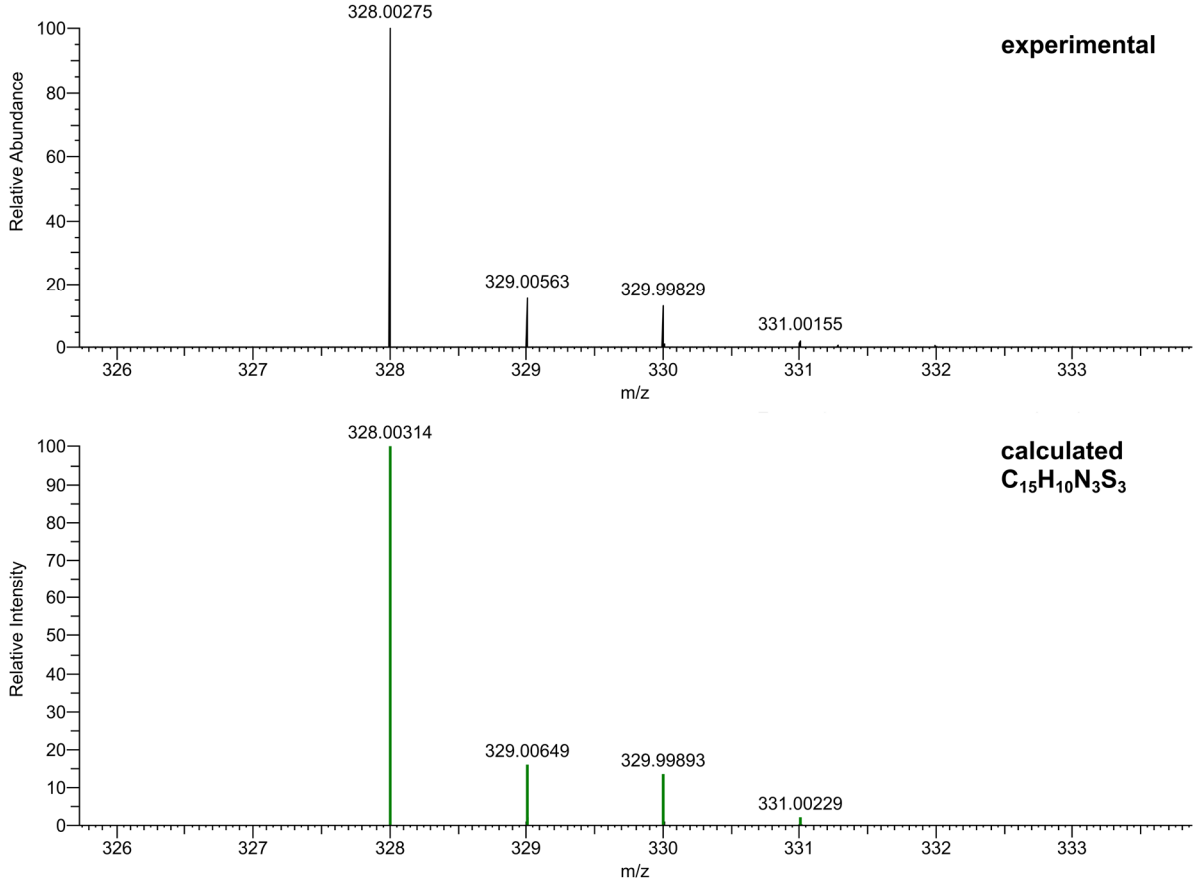

Figure S 6: Mass spectrum of Thiacalix[3](2,6)pyridine (Py_3S_3) (**2**) with the isotopic pattern of the molecular peak $[M\text{-}H]^+$.

2.7 IR and Raman spectroscopy of $[Mo(CO)_3(Py_3S_3)]$ (1)

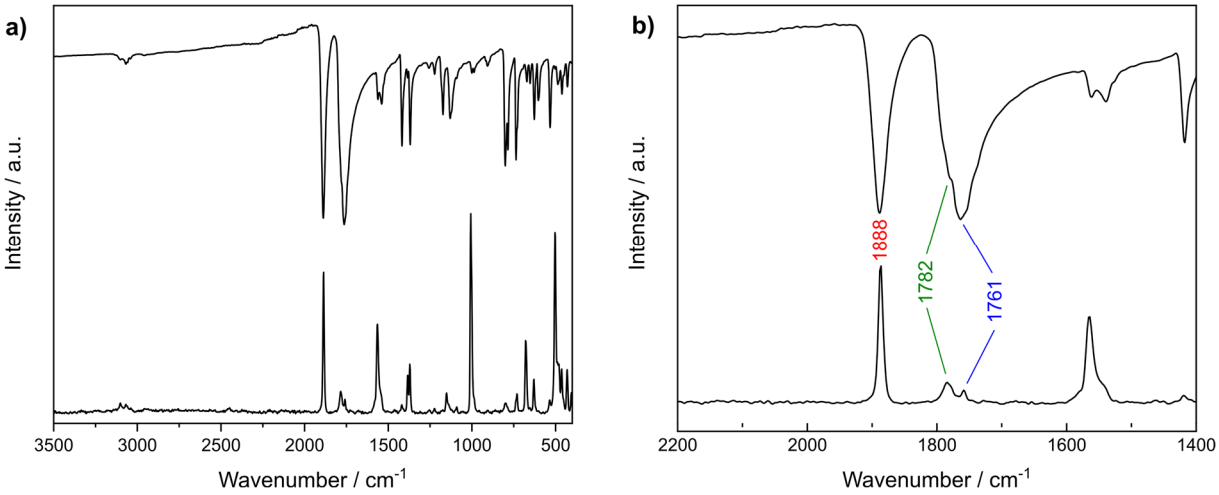

Figure S 7: a) IR and Raman spectra of $[Mo(CO)_3(Py_3S_3)]$ (**1**) between 3500 cm^{-1} and 400 cm^{-1}. The Raman data were multiplied with the factor of 30; **b)** Enlargement of the carbonyl vibrations region between 2200 cm^{-1} and 1400 cm^{-1}.

2.8 IR and Raman spectroscopy of Thiacalix[3](2,6)pyridine (Py_3S_3) (2)

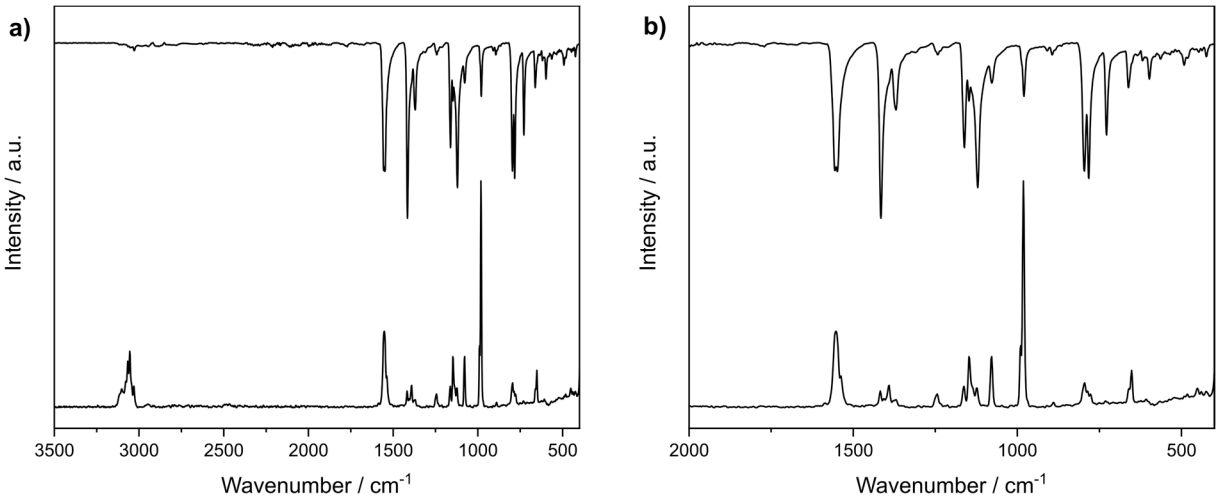

Figure S 8: a) IR and Raman spectra of the Thiacalix[3]pyridine ligand (Py_3S_3)] (**2**) between 3500 cm^{-1} and 400 cm^{-1}. The Raman data were multiplied with the factor of 2; **b)** Enlargement of the vibrations region between 2000 cm^{-1} and 400 cm^{-1}.

3 Single Crystal X-Ray Structure Determination

Table S 1: Selected crystal data and results of the structure refinement for compound **1**.

Empirical formula	$C_{19}H_{12}MoN_3O_{3.5}S_{3.5}$
Formula weight	546.47
Temperature/K	100(2)
Crystal system	monoclinic
Space group	*C*2/*c*
a/Å	33.1665(2
b/Å	10.32120(10)
c/Å	12.45270(10)
α/°	90
β/°	109.4270(10)
γ/°	90
Volume/Å^3	4020.09(6)
Z	8
ρ_{calc}g/cm^3	1.806
μ/mm^{-1}	0.014
Crystal size/mm^3	0.15 × 0.03 × 0.03
2Θ range for data collection/°	5.65 to 160.064
Index ranges	-42 ≤ h ≤ 42, -11 ≤ k ≤ 13, -15 ≤ l ≤ 15
Reflections collected	61942
Independent reflections	4358
$R_{int.}$	0.0227
Reflections with [I>=2σ (I)]	4324
Parameters	487
Goodness-of-fit on F^2	1.0674
Final R indexes [I>=2σ (I)]	R_1 = 0.0253, wR_2 = 0.0662
Final R indexes [all data]	R_1 = 0.0254, wR_2 = 0.0664
Largest diff. peak/hole / e Å^{-3}	0.37/-0.38

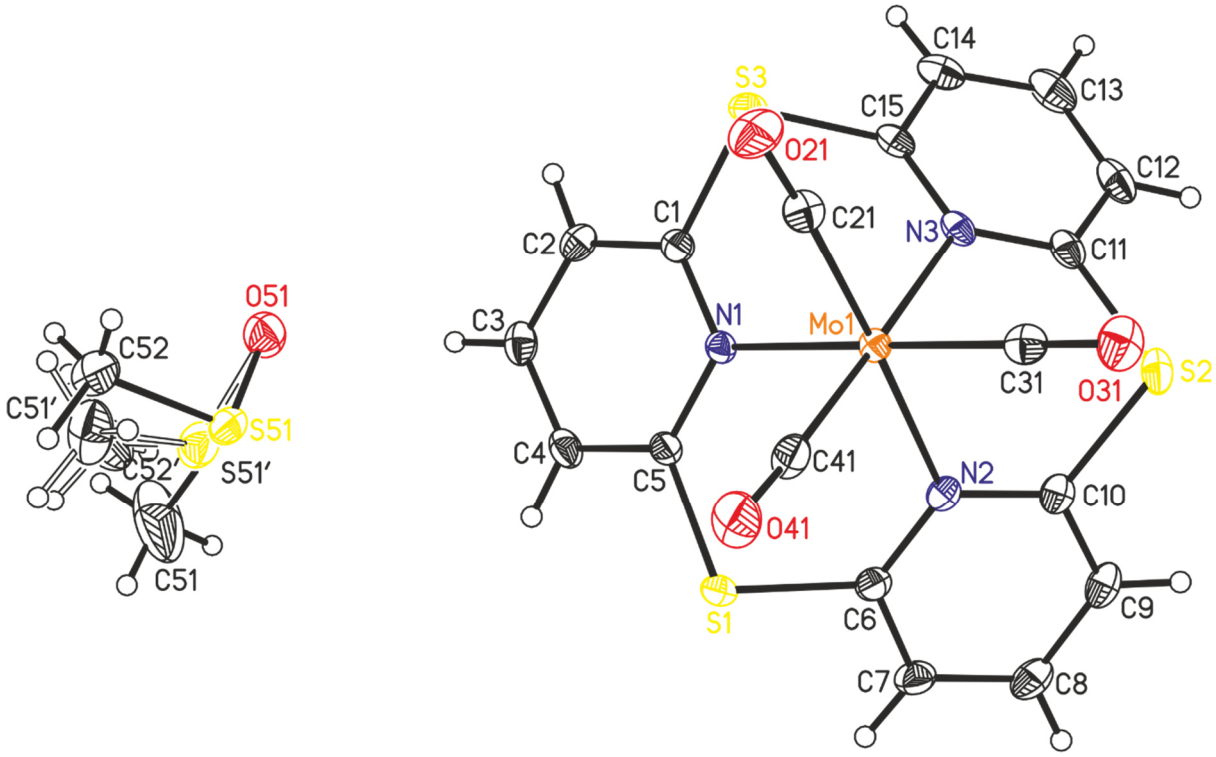

Figure S 9: Crystal structure of compound **1** with labeling and displacement ellipsoids drawn at the 50% probability level. The disorder of the DMSO molecule is shown with full and open bonds.

4 Infrared Reflection Absorption Spectroscopy – IRRAS

4.1 Original PM-IRRAS spectrum of $[Mo(CO)_3(Py_3S_3)]$ (1) with Bessel function

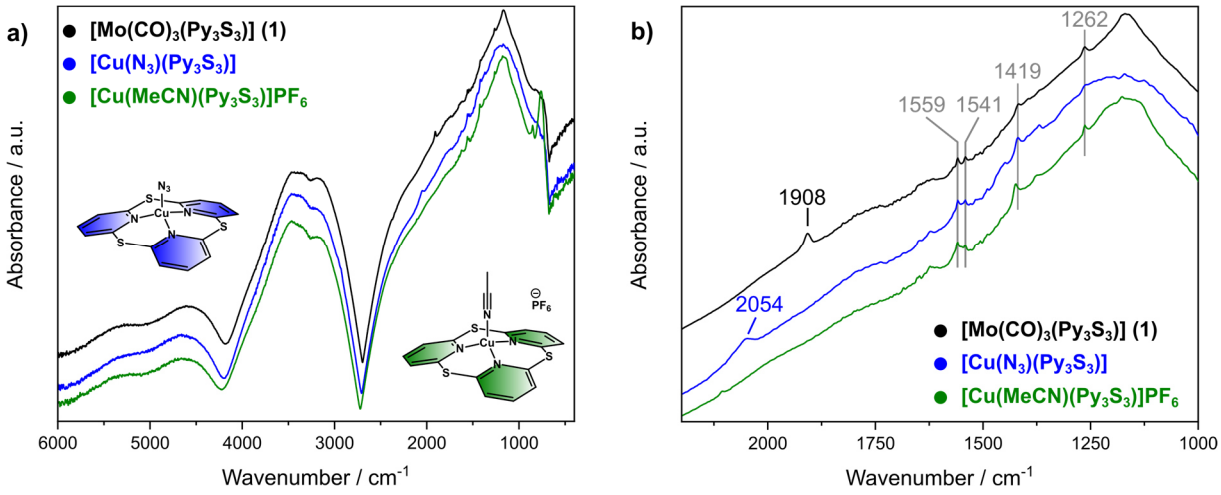

Figure S 10: Shown are the measured PM IRRA spectra with Bessel function of $[Mo(CO)_3(Py_3S_3)]$ (**1**) and two copper(I) complexes with azide or acetonirile using the thiacalixpyridin ligand **2** as well. **a)** Full PM IRRA spectra between 6000 cm^{-1} and 400 cm^{-1}. b) Enlargement of the area between 2200 cm^{-1} and 1000 cm^{-1}. It shows, that (independent of the metal center) in adsorbed complexes using the thiacalixpyrindin **2** four characteristic ligand vibrations can be observed at 1559 cm^{-1}, 1541 cm^{-1}, 1419 cm^{-1} and 1262 cm^{-1}, which are visualized by the grey lines.

Figure S10 shows the original IRRA spectrum of complex $[Mo(CO)_3(Py_3S_3)]$ (**1**) with Bessel function (black line). In Figure 4 of the manuscript the evaluated spectrum without the Bessel function is shown. Additionaly, the IRRA spectra of two other complexes using the thiacalixpyridine **2** as ligand are shown as well. Hereby, the blue spectrum corresponds to the copper(I) azide complex and the green line represents the copper(I) acetonitrile complex with hexafluorophosphate as counterion.

In the evaluated spectrum (Figure 4) two sharp absoprtion bands can be identified at 1541 cm^{-1} and 1262 cm^{-1}. However, in the calculated IRRA spectrum for complex **1** these vibrations do not appear. The calculation is performed without the underlying metal surface (see details below in chapter 9.2). The adsorbed complex molecules interact with the surface, which maybe results in a change of the TDM proportion along the z-axis of this vibrational mode. Additionally, the direct interaction of the pyridine rings with the underlying metal atoms could result in different vibrational modes compared to the gas phase (single molecule structure) calculation. Unfortunalety, we are limited in this area of DFT calculations with surfaces. Further investigations should be done at this point.

To demonstrate, that these two absorptions bands at 1541 cm^{-1} and 1262 cm^{-1} are characteristic vibrations for adsorbed complexes using the thiacalixpyridine ligand **2**, the IRRA spectrum of the two copper(I) complexes are shown in figure S10 as well.

4.2 Orientation of the transition dipole moments of the CO vibrational modes

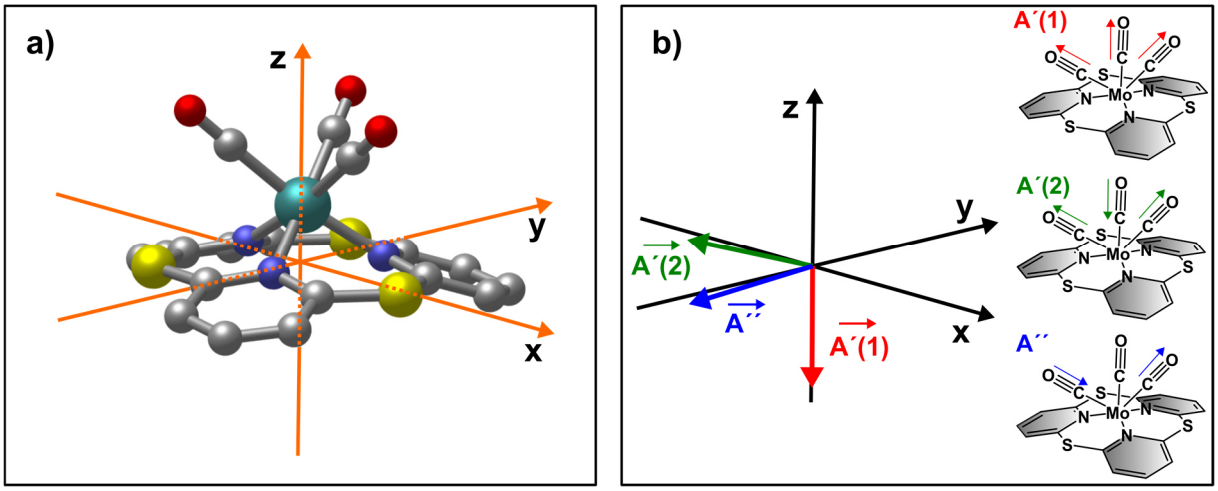

Figure S11: a) The position of the complex $[Mo(CO)_3(Py_3S_3)]$ (**1**) in the coordinate system is shown. Hereby, the three nitrogen donor atoms lay in the xy plane. **b)** The orientation of the transition dipole moment (TDM) vectors of the three vibration modes (A´(1) red, A´(2) green and A´´ blue, see on the right hand side) of the CO ligands in the coordinate system are shown. These TDM vectors were calculated by DFT.

In the IRRA spectroscopy the orientation of the transition dipol moment (TDM) of a certain vibration is important due to the surface selection rule. Hereby, the vibrational modes with a component in z direction will be reinforced and the intensity of vibrational modes oriented in the xy plane (parallel to the surface) are vanished.

The complex $[Mo(CO)_3(Py_3S_3)]$ (**1**) posesses three vibrational modes for the CO ligands. DFT calculations shows that the TDM´s of the vibration A´(1), A´(2) and A´´ are orthogonal to each other. When the complex **1** is so oriented that the three nitrogen donor atoms are alligned in the xy plane (see Figure S11a), than the TDM vector of the total symmetric vibration A´(1) is nearly perfectly alligned to the z-axis. The TDM vectors of the two other vibrational modes are mostly alligned to the x-axis (A´(2) mode) and to the y-axis (A´´ mode), respectively (see Figure S11b).

In the following the coordinates of the TDM vectors for the three vibrational modes of the CO ligands and the angles between these vectors are listed.

$$\overrightarrow{A´(1)} = \begin{pmatrix} -0.1414 \\ -0.0497 \\ -46.898 \end{pmatrix} \; ; \; \overrightarrow{A´(2)} = \begin{pmatrix} -31.185 \\ -3.7821 \\ 0.1896 \end{pmatrix} \; ; \; \overrightarrow{A´´} = \begin{pmatrix} 3.5630 \\ -31.362 \\ 0.1168 \end{pmatrix}$$

$$\alpha\,(\overrightarrow{A´(1)} \leftrightarrow \overrightarrow{A´(2)}) = 90.167°$$

$$\beta\,(\overrightarrow{A´(1)} \leftrightarrow \overrightarrow{A´´}) = 90.171°$$

$$\gamma\,(\overrightarrow{A´(2)} \leftrightarrow \overrightarrow{A´´}) = 89.565°$$

4.2 Vibrational analysis of $[Mo(CO)_3(Py_3S_3)]$ (1)

Table S 2: A full vibrational analysis with vibration assignment is shown in the range of 3000 cm^{-1} to 750 cm^{-1} for the carbonyl complex **1**. The energies of the calculated spectrum were corrected by using the equation: $V_{corr.} = (V_{calc.} / 1.18154) + 179.64\ cm^{-1}$.

Mode	calc. freq. uncorr.	calc. freq. corr.	calc. Int. IR	calc. Int. IRRAS	Bulk IR	IRRAS	TDM	Assignment
1	686.1	760.3	13.90	13.89			⊥	In plane deformation
2	689.0	762.8	2.45	0.00			=	In plane deformation
3	689.5	763.2	2.51	0.02			=	In plane deformation
4	756.3	819.7	7.87	3.44			/	asym. C-H wagging
5	757.5	820.7	6.65	0.01			=	asym. C-H wagging
6	761.3	824.0	74.39	73.94	801		⊥	sym. C-H wagging
7	807.7	863.2	18.52	0.36			/	asym. C-H wagging
8	808.4	863.8	18.13	0.00			=	asym. C-H wagging
9	813.5	868.2	0.01	0.00			=	In plane deformation
10	819.5	873.2	25.03	24.96	908		⊥	sym. C-H wagging
11	828.5	880.9	8.48	0.00			=	In plane deformation
12	828.9	881.1	7.74	0.01			=	In plane deformation
13	930.2	966.9	0.03	0.00			=	asym. C-H wagging
14	932.6	968.9	0.20	0.00			=	asym. C-H wagging
15	933.6	969.8	0.20	0.00			=	asym. C-H wagging
16	1007.4	1032.2	1.78	0.00			=	sym. C-H wagging
17	1008.0	1032.8	2.33	0.00			=	sym. C-H wagging
18	1008.6	1033.3	0.37	0.08			/	sym. C-H wagging
19	1020.2	1043.0	11.77	0.00			=	In plane deformation
20	1020.6	1043.4	12.30	0.03			=	In plane deformation
21	1031.3	1052.5	20.16	20.15	1001		⊥	In plane deformation
22	1117.2	1125.2	0.20	0.00			=	C-H bending py
23	1117.3	1125.2	0.24	0.00			=	C-H bending py
24	1120.3	1127.8	0.99	0.99			⊥	C-H bending py
25	1161.8	1162.9	0.09	0.00			=	C-H bending py
26	1164.8	1165.5	28.86	0.01	1130		=	C-H bending
27	1164.9	1165.5	27.25	0.01			=	C-H bending
28	1171.7	1171.3	29.21	0.00			=	C-H bending
29	1171.8	1171.4	32.31	0.00			=	C-H bending
30	1189.0	1185.9	5.55	5.55			⊥	In plane deformation
31	1193.4	1189.6	0.05	0.00			=	C-H bending
32	1198.9	1194.3	14.56	0.00	1174		=	C-H bending
33	1199.2	1194.5	13.64	0.01			=	C-H bending
34	1295.8	1276.3	0.08	0.01		1262	=	asym. C=N=C stretching
35	1296.4	1276.8	0.04	0.00			=	asym. C=N=C stretching

36	1302.2	1281.7	0.00	0.00			=	asym. C=N=C stretching
37	1409.3	1372.4	110.74	0.03	1369		=	sym. C=N=C stretching
38	1409.6	1372.7	111.50	0.16			=	sym. C=N=C stretching
39	1423.5	1384.4	67.94	0.14	1385		=	sym. C=N=C stretching
40	1443.3	1401.1	0.05	0.00			=	asym. C=C stretching
41	1457.8	1413.5	41.56	41.32	1419	1419	⊥	asym. C=C stretching
42	1457.9	1413.6	41.91	41.74			⊥	asym. C=C stretching
43	1583.8	1520.1	0.00	0.00			=	C=C stretching
44	1596.7	1531.0	10.43	0.01			=	C=C stretching
45	1597.5	1531.7	11.16	0.00			=	C=C stretching
46	1617.1	1548.2	0.77	0.03	1540	1541	/	asym. C=C stretching
47	1617.4	1548.6	1.12	0.00			=	asym. C=C stretching
48	1626.0	1555.8	10.84	10.82	1561	1559	⊥	sym. C=C stretching
49	1960.9	1839.3	996.2	0.01	1761		=	C-O stretching A´´
50	1962.3	1840.4	986.8	0.04	1782		=	C-O stretching A´(2)
51	2034.2	1901.3	2199.4	2199.4	1888	1908	⊥	C-O stretching A´(1)
52	3205.6	2892.7	1.11	0.03	3042		=	asym. C-H stretching
53	3205.7	2892.8	1.12	0.01			=	asym. C-H stretching
54	3205.9	2892.9	0.38	0.22			/	asym. C-H stretching
55	3225.1	2909.2	0.02	0.00	3059		=	asym. C-H stretching
56	3225.7	2909.7	0.04	0.00			=	asym. C-H stretching
57	3225.8	2909.8	0.04	0.00			=	asym. C-H stretching
58	3229.9	2913.2	0.48	0.05	3102		/	sym. C-H stretching
59	3230.3	2913.6	0.47	0.04			/	sym. C-H stretching
60	3230.4	2913.7	0.38	0.09			/	sym. C-H stretching

⊥ : TDM is perpendicular to the surface oriented

/ : TDM is skew to the surface oriented

= : TDM is parallel to the surface

5 Scanning Tunneling Microscope - STM

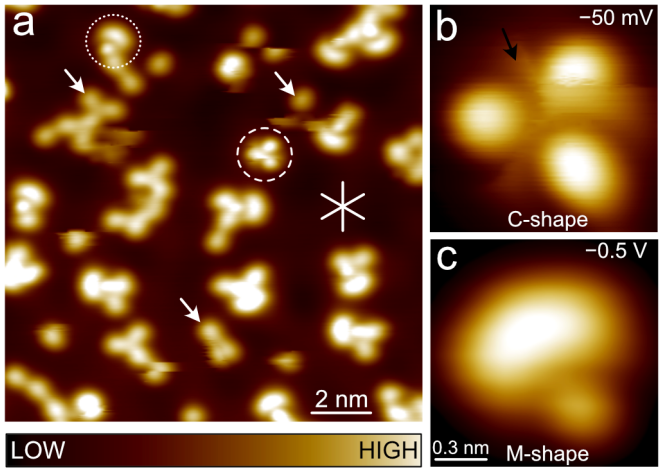

Figure S 12: (a) Constant-current topograph (-50 mV, 30 pA) of [Mo(CO)3(Py3S3)] molecules deposited on Au(111). Intact molecules exhibit two distinct shapes marked by dotted (M-shape) and dashed circles (C-shape). White arrows indicate examples of irregular structures that may be fragments of the deposited complexes. White lines denote the close-packed directions of the (111) substrate lattice. (b) and (c) show more detailed images of an isolated complex, whose contrast varies at different imaging parameters. Set points: (b) −50 mV, 100 pA and (c) −500 mV, 30 pA. Molecules in aggregates, for example the complex indicated with a dotted circle in (a), did not show this effect. They exhibited an M-shape over a range of imaging parameters.

Figure S12 shows topographs of the complex on Au(111). In an overview image (Figure S12a) we observe protrusions either as individual entities or in clusters. Some examples are marked by the white arrows. We attribute these structures to the fragments of decomposed molecules. The supposed fragments tend to be mobile under the influence of the tip. As a consequence, a detailed study of, e. g., the voltage dependence of their images was not feasible. They can also affect the images of the more stable, intact molecules because they may be accidentally moved toward or away from them.

On the Au(111) surface, we observed two different shapes on the intact molecules, namely an approximately threefold symmetric, clover-like pattern (C-shape) and mushroom-like shape (M-shape), as shown in Figures S12b and c. Molecules in aggregates (example indicated by a dotted circle in Figure S12a) usually exhibit an M-shape at different sample voltages. Isolated molecules usually appear M-shaped at elevated voltages and C-shaped at low bias, regardless of the voltage polarity. The three lobes of C-shaped molecules exhibit similar heights with respect to the surface (≈ 220 pm in Figure S13a). In each of the interspaces between the lobes an elongated feature is observed that exhibits instabilities during imaging. On the M-shape molecules (Figure S13b), the larger lobe (brown arrow) is usually ≈ 20 pm higher than the smaller one (blue arrow).

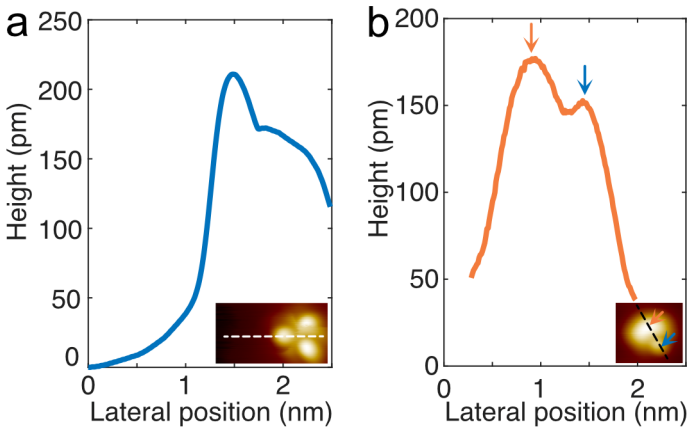

Figure S 13: Profile of a C-shaped (a) and an M-shaped (b) molecule along the dashed line shown in each inset. Set points for the insets: (a) −50 mV, 100 pA, (b) −500 mV, 30 pA.

6 X-Ray Photoelectron Spectroscopy – XPS

6.1 XPS measurements of [$Mo(CO)_3(Py_3S_3)$] (1) on Au(111)

6.1.1 Monolayer on Au(111)

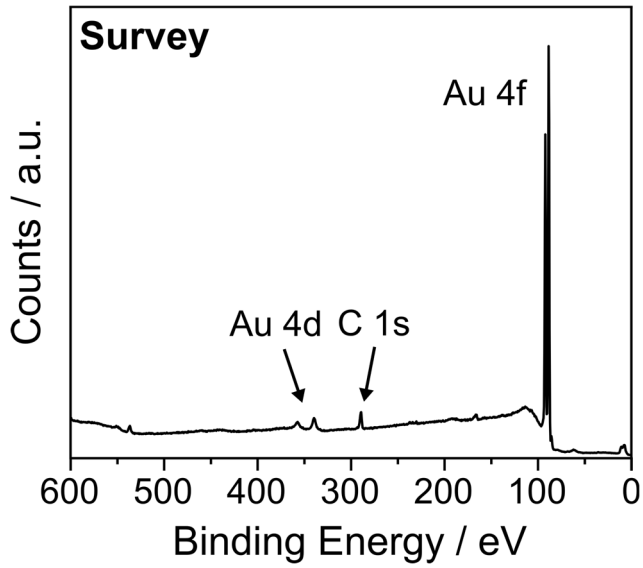

Figure S 14: Survey spectrum of the $Mo(CO)_3(Py_3S_3)$] (**1**) monolayer on Au(111).

Table S 3: Fitting Parameter for the XP spectra of the $Mo(CO)_3(Py_3S_3)$] (**1**) monolayer on Au(111).

Component	Signal	Binding Energy / eV	Area / %	fwhm
S-different thiolate	S 2p	161.3 / 162.4	35	0.7
S-Au	S 2p	162.2 / 163.3	16	0.7
S-Thioether	S 2p	164.1 / 165.2	49	0.8
C-C	C 1s	285.1	53	1.0
C-N	C 1s	285.6	35	1.0
C-O	C 1s	286.8	12	1.1
Mo	Mo 3d	227.6 / 230.7	37	0.9
Mo	Mo 3d	228.8 / 231.9	19	1.0
Mo	Mo 3d	229.8 / 232.9	44	1.0
Pyridine	N 1s	400.2	100	1.2

6.1.2 Thicklayer on Au(111)

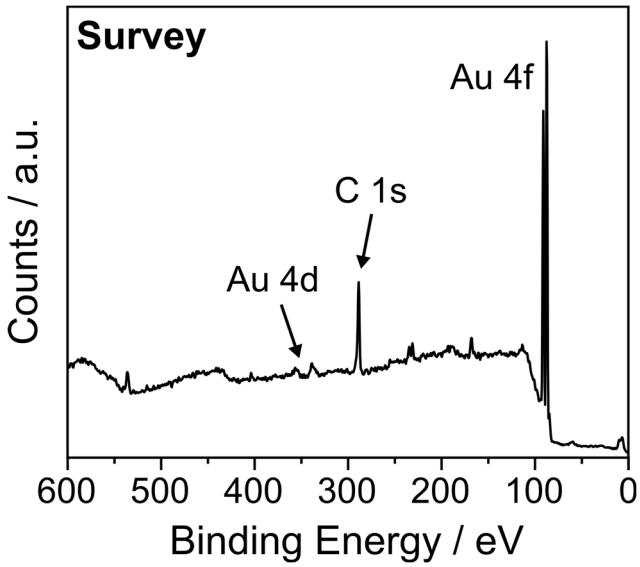

Figure S 15: Survey spectrum of the $Mo(CO)_3(Py_3S_3)$] (**1**) monolayer on Au(111).

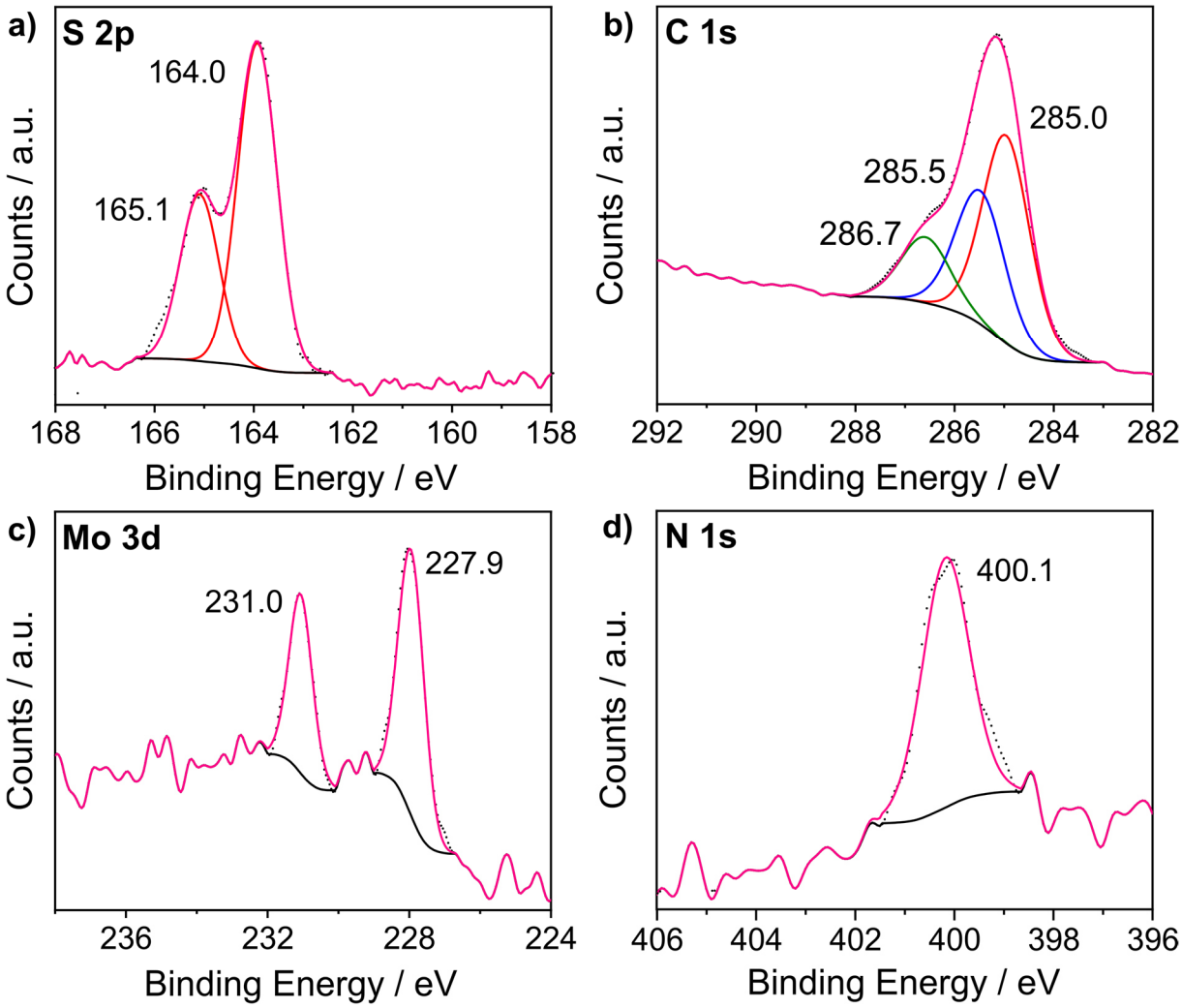

Figure S 16: S 2p (a), C 1s (b), Mo 3d (c) and N 1s (d) XP spectra of a thicklayer of [$Mo(CO)_3(Py_3S_3)$] (**1**) on Au(111).

Figure S 15 and S 16 shows the XP spectra of a thicklayer of $Mo(CO)_3(Py_3S_3)$] (**1**) on Au(111). The Survey spectrum (Figure S 15) shows the Au4f lines at 84.0 eV and 87.5 eV as main signal. The second large signal is the C 1s peak at 285.0 eV. The intensity ratio to the Au 4d signals at 335.5 eV and 354.0 eV shows that there is a thick layer on the surface.[15–17,18]

The element spectra for S 2p, Mo 3d and N 1s each contains a single signal set. In the S 2p spectrum (Figure S 16a) a doublet at 164.0 eV and 165.1 eV is present, which has the typical splitting of 1.1-1.2 eV and a intensity area ration of 2:1.[19] This signal belongs to the bridging sulphur atoms of the ligand scaffold. The spectrum of Mo 3d (Figure S 16c) contains a single species. The signal has a doublet ratio of 3:2 and the typical splitting of 3.0-3.1 eV.[15–17] The species at 227.9 eV and 231.0 eV is assigned to molybdenum(0) of the complex **1**. The N 1s spectrum (Figure S16d) shows only one signal at 400.1 eV, which represents the pyridine nitrogen atoms.[15,17]

The C 1s spectrum (Figure S 16b) contains three signals. The main species at 285.0 eV (red line) belongs to the carbon atoms which are bonded to other carbon atoms. The second signal at 285.5 eV (blue trace) is assigned to the carbon atoms which are bound to hteroatoms (C-N). The third species at 286.7 is assigned to the carbon atoms of the carbonyl ligands.[16] The intensity ratios of the three species is 50:34:16 and fits almost perfectly with the theoretical value of 50:33:17.

The XP spectra of the thick layer of $Mo(CO)_3(Py_3S_3)$] (**1**) shows the binding energy of each different atom species and forms an excellent basis for the interpretation of the monolayer XP spectra (see manuscript).

Table S 4: Fitting Parameter for the XP spectra of the $Mo(CO)_3(Py_3S_3)$] (**1**) thicklayer on Au(111).

Component	Signal	Binding Energy / eV	Area / %	fwhm
S-Thioether	S 2p	164.0 / 165.1	100	0.9
C-C	C 1s	285.0	50	1.1
C-N	C 1s	285.5	34	1.1
C-O	C 1s	286.7	16	1.1
Mo	Mo 3d	227.9 / 231.0	100	0.8
Pyridine	N 1s	400.1	100	1.1

6.2 Flipping of the bridging sulfur atom towards the Au(111) surface

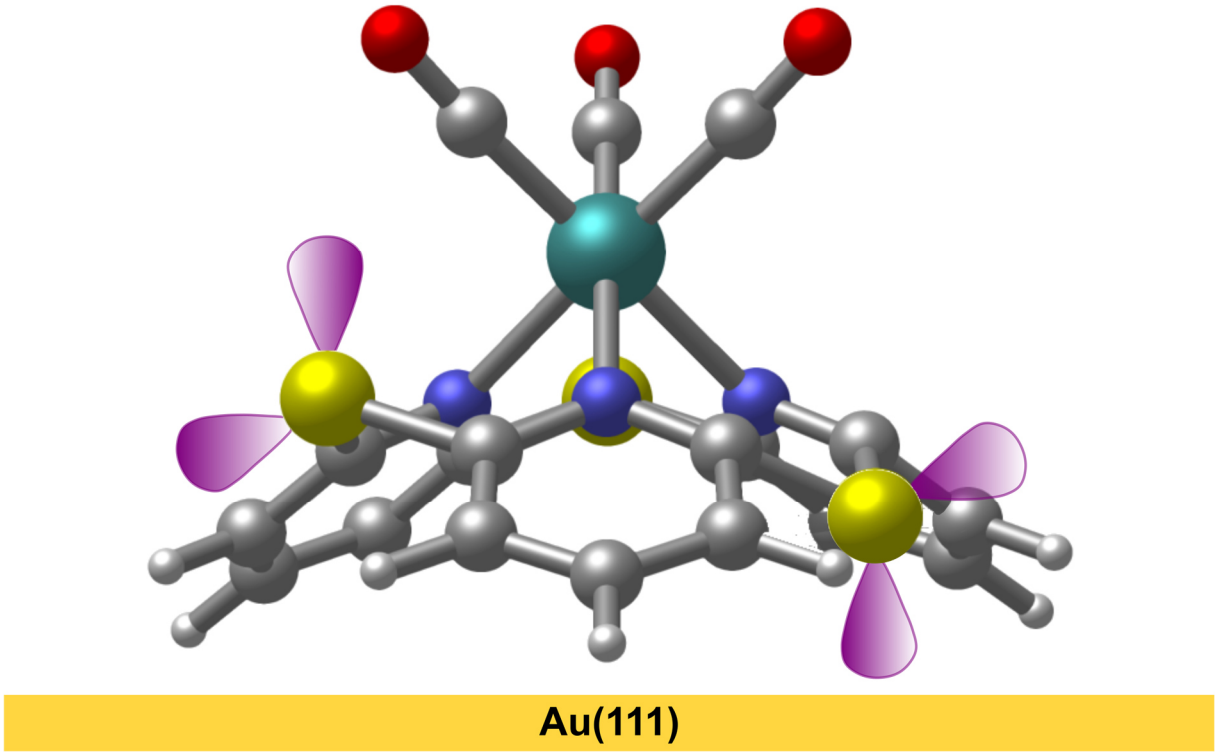

Figure S 17: Flipping of the bridging right sulfur atom towards the Au(111) surface. The two lone pairs of the sp^3 hybridized sulfur atoms are shown in violet. If the sulfur bridge are above the plane of the pyridine carbon atoms the lone pairs can not interact with the gold surface. However, if the bridging sulfur atom flip under the plane of the bridged pyridine carbon atoms one lone pairs is located directly towards the gold surface and interact with the gold atoms to form a covalent Au-S bond.

7 Near Edge X-Ray Absorption Fine Structure - NEXAFS

7.1 Theoretical determination of the angles of π* orbitals of [Mo(CO)$_3$(Py$_3$S$_3$)] (1)

The transition dipole moment T of a π* orbital is perpendicular to the bonding plane. Due to the parallel orientation of the basal plane of the [Mo(CO)$_3$(Py$_3$S$_3$)] (**1**) complex on an Au(111) surface, the approximate angles (α' and γ') of the bonding plane of the atoms can be determined using the angles from the crystal structure. The angle of the transition dipole moment T to the surface normal n for the C- and N-atoms of the pyridine rings (α) and the C atoms of the carbonyl ligands (γ) is then determined by applying the equations (see S7-1 to S7-2 and Figure S16c) (Note that due to the aromaticity of pyridine, the π* orbitals of all atoms of the ring are oriented in a plane and therefore have the same angle to the surface normal). The data determined are summarised in Table S5.

$$\alpha = 90° - \alpha' \tag{S7-1}$$

$$\gamma = 90° - \gamma' \tag{S7-2}$$

Table S 5: Theoretical determine values of the π* orbitals of [Mo(CO)$_3$Py$_3$S$_3$)] (**1**).

	C- and N-atoms pyridine		C atoms carbonyl	
angle	α	α´	γ	γ´
value	46-48°	42-44°	47-49°	41-43°

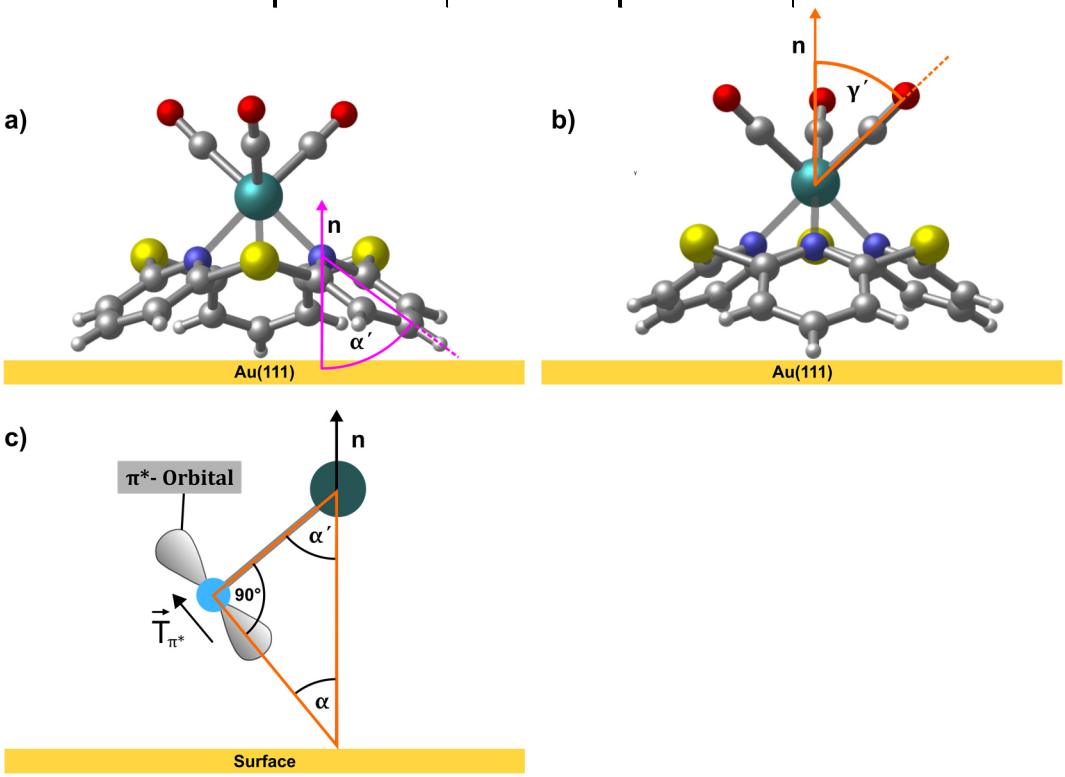

Figure S 18: Schematic representation of the determination of the angles (α´and γ´) from the bond plane of the atoms of the pyridine ring (a) and the C atoms of the carbonyl ligands (b) to the surface normal n; c) shows the schematic relationship of the angle α´ of the bond plane to the angle α of the transition dipole moment T of a π* transition to the surface normal n.

7.2 Graphical determination of the angle α of the π* orbitals of the pyridines in [Mo(CO)$_3$(Py$_3$S$_3$)] (1)

The intensities of the resonance at 285.7 eV in the C-NEXAFS spectrum and the resonance at 400.1 eV in the N-NEXAFS spectrum was used to determine the angle α (orientation) of the π* orbitals of pyridine in [Mo(CO)$_3$(Py$_3$S$_3$)] (**1**) towards the surface normal n.

The intensities at different angles of incidence θ were multiplied by a factor so that they fit as well as possible to one of the theoretical curves calculated according to equation S7-3.[20] The polarization P of the beamline was also taken into account with P = 0.91.

Note here, that the determined angle α represents an average angle: it does not mean that all molecules are aligned in this way, but it is a statistical average.

Figure S17 shows the graphical determination of the angle α of the π* orbitals of the pyridine atoms and in Table S6 the intensities of the resonance are listed.

$$I = P \cdot cos^2(\theta) \cdot \left(1 - \frac{3}{2} \cdot sin^2(\alpha)\right) + \frac{1}{2} \cdot sin^2(\alpha) \qquad \text{(S7-3)}$$

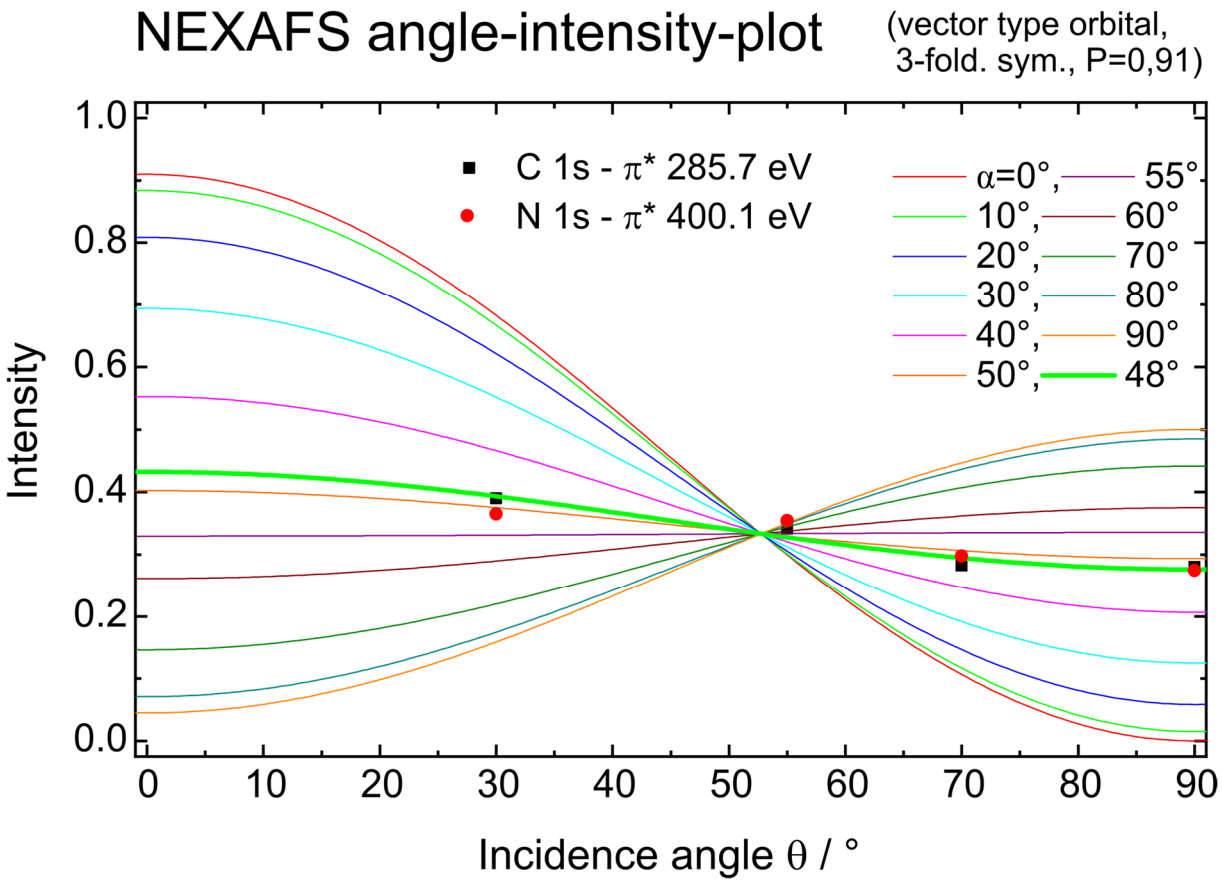

Figure S19: Graphical determination of the angle α of the π* orbitals of the pyridine atoms towards the surface normal n. The black quadrats corresponds to the resonance of C 1s - π* at 285.7 eV and the red dots to the resonance of N 1s - π* at 400.1 eV. The bold green line represents the theoretical curve, which best represents the measured values when α = 48°.

Table S 6: Measured and normalized intensities of the C 1s – π* at 285.7 eV and N 1s – π* at 400.1 eV resonances of $[Mo(CO)_3(Py_3S_3)]$ (**1**).

	Intensity C 1s – π* at 285.7 eV		Intensity N 1s – π* at 400.1 eV	
θ	measured	normalized	measured	normalized
30°	0.90720	0.39010	0.70183	0.36495
55°	0.79312	0.34104	0.68166	0.35446
70°	0.65726	0.28262	0.57241	0.29765
90°	0.65131	0.28006	0.52797	0.27454

8 Reactivity towards oxygen (O_2)

8.1 Investigation of the reactivity of [Mo(CO)$_3$(Py$_3$S$_3$)] (1) towards oxygen (O_2) in solution

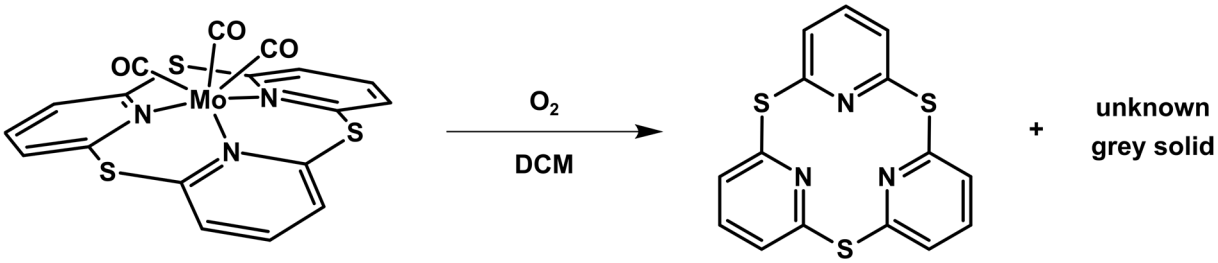

1 **2**

Scheme S 1: Reaction of [Mo(CO)$_3$(Py$_3$S$_3$)] (**1**) with oxygen O_2 in dichloromethane solution produces the thiacalixpyridine ligand **2** and a unknown grey solid.

The carbonyl complex [Mo(CO)$_3$(Py$_3$S$_3$)] (**1**) (100 mg, 197.1 µmol) was placed in a schlenk flask. The inert atmosphere was replaced by a 100% oxygen atmosphere. The complex **1** was dissolved in 16 mL of dry dichloromethane. The solution was stirred at room temperature for 168 h. Over this period the red solution slowly turns darker until a black suspension was formed at the end. The suspension was filtered and the dark grey/black solid was washed with 10 mL of dichloromethane and dried under vacuum. The solvent of the filtrate was removed by vacuum, yielding a white solid.

Yield: 17 mg of grey solid and 53 mg of white solid.

The white solid was investigated by ^{1}H-NMR. Apart from a few impurities, the spectrum in Figure S20 otherwise only shows the signals from the free thiacalixpyridine ligand **2**. This means during the reaction of **1** with oxygen a demetallation process occurred.

The grey solid was investigated by XRD pattern. The spectrum is shown in Figure S21. The grey solid is amorphous with a low crystalline content. After 14 hours of measurement, some signals can be detected. After comparison with the XRD pattern of molybdenum metal, molybdenum(IV)oxide (MoO_2) and molybdenum(VI)oxide (MoO_3), the grey solid is not one of the compounds mentioned above.

The IR spectrum of the gray solid is shown in Figure S22. It contains absorption bands that would fit well with the thiacalixpyridine ligand in comparison with complex **1** and ligand **2** (1557 cm^{-1}, 1419 cm^{-1}, 1386 cm^{-1}, 1164 cm^{-1}, 1137 cm^{-1}). The bands at 1474 cm^{-1} and 1255 cm^{-1} cannot be assigned to the thiacalix ligand **2**. In addition, the absorption spectrum is characterized by a consistently strong absorption below the band at 947 cm^{-1}. This could be the absorption of molybdenum oxides, which are characterized by strong IR absorption in this range.[21]

Ultimately, it was not possible to determine exactly what the grey solid was. In any case, compared to the azakalixpyridine system,[17,22] no defined oxidation product was formed, but mainly a demetallation occurred.

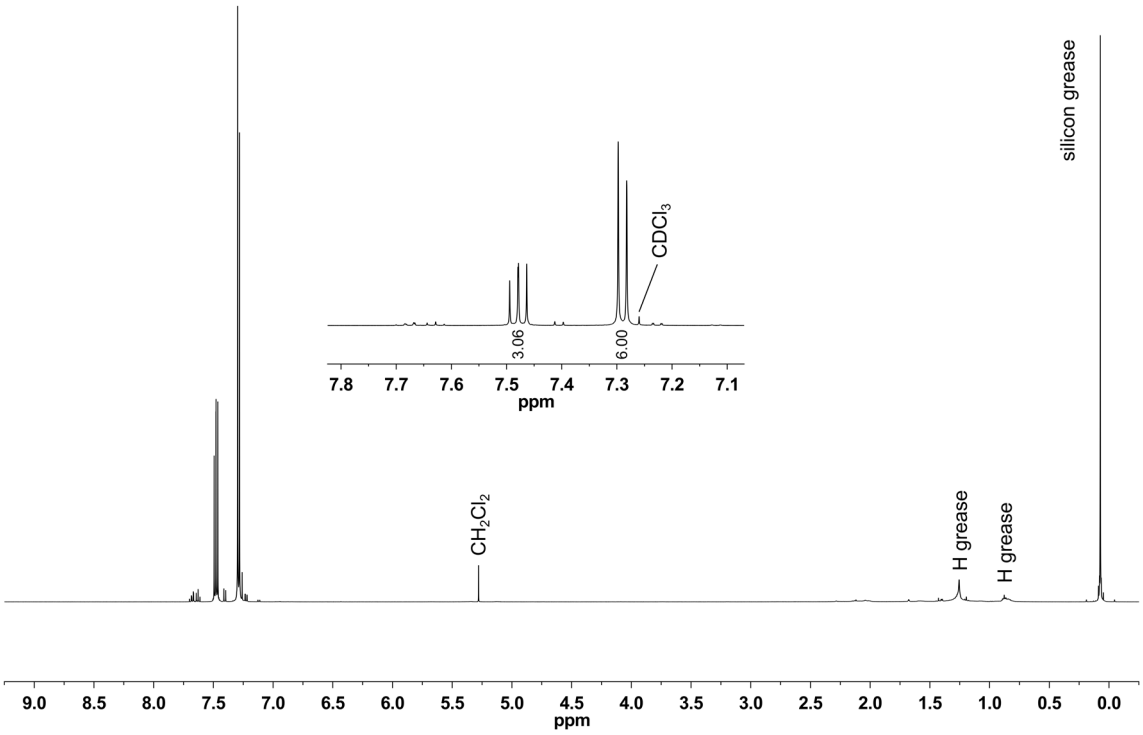

Figure S20: ^{1}H-NMR of the filtrate after reaction of [Mo(CO)$_3$(Py$_3$S$_3$)] (**1**) with oxygen O_2. Apart from a few impurities, the spectrum otherwise only shows the signals from the free thiacalixpyridine ligand **2**.

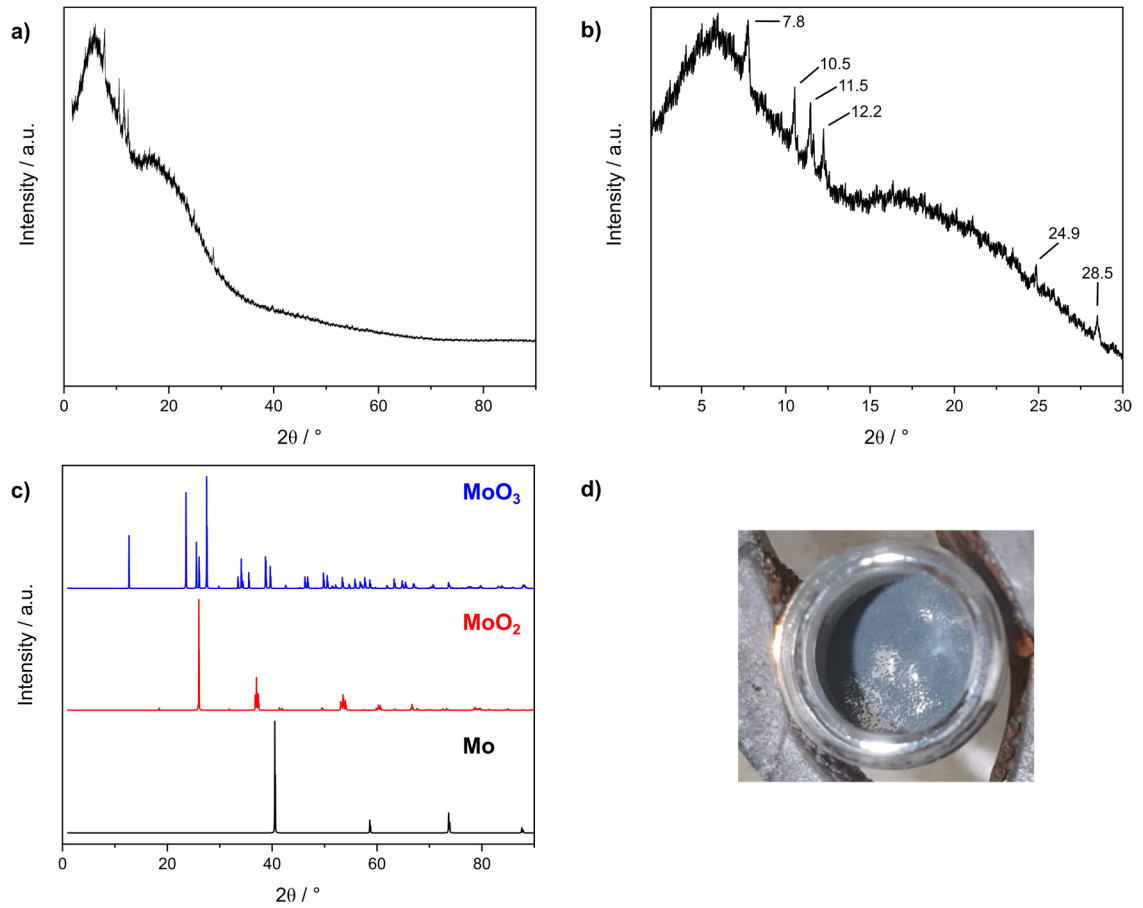

Figure S21: a) XRD pattern spectrum from 1.5° to 90°; b) enlargement of the region between 2° and 30° with the main signals; c) calculated XRD pattern spectrum of molybdenum metal, molybdenum(IV)oxide and molybdenum(VI)oxide; d) picture of the grey solid received.

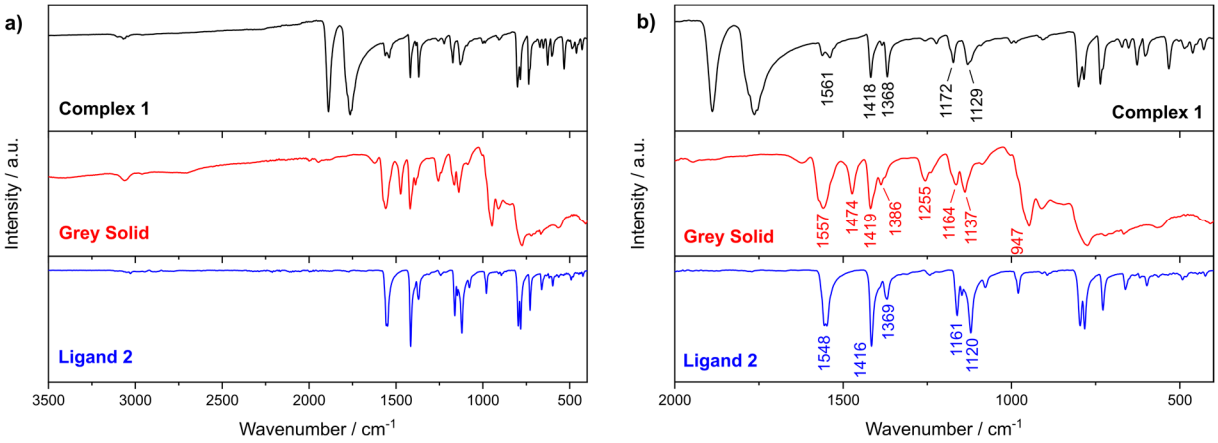

Figure S22: Comparison of the IR spectra of the complex 1 (black) and the ligand 2 (blue) with the IR spectrum of the grey solid (red) obtained in the oxidation experiment with O_2; a) spectra in the range from 3500 cm^{-1} to 400 cm^{-1}; b) spectra in the range of 2000 cm^{-1} to 400 cm^{-1}.

8.2 Investigation of the reactivity of $[Mo(CO)_3(Py_3S_3)]$ (1) towards oxygen (O_2) adsorbed on a Au(111) surface under radiation with 365 nm

To investigate the reactivity of $[Mo(CO)_3(Py_3S_3)]$ (**1**) towards oxygen adsorbed on a Au(111) surface under radiation with 365 nm, the IRRA spectroscopy was used. Hereby, the Bessel function was chosen such that the PEM maximum efficiency was set for the half-wave at 1750 cm^{-1}. Hereby, the carbonyl band are clearly visible with high intensity and on the other hand the bands in the finger print region are also distingly seen. The measured spectrum of the carbonyl complex at the beginning represents the intensity at time t = 0 min (black curve, see Figure S23). Immediately after the addition of oxygen, the stopwatch was started and the exposure was switched on at the same time. To determine the relative change in the characteristic bands, the spectra were set to 0 with the Bessel function at 2000 cm^{-1}. The respective intensity of the bands at time t was then selected. In order to determine the relative change in intensities to each other, the spectrum was evaluated at the beginning and at the end of the measurement by removing the Bessel function. The intensity at the beginning was set to the value 1 and the remaining intensity of the bands at the end of the measurement was related to this.

The evolution of the intensity from the carbonyl band at 1908 cm^{-1} shows a monoexponential decay. The data points were fitted using the equation S8-1 and the fitting parameter a listed in table 7.

$$y = y_0 + A_1 \cdot exp^{-\frac{x}{t_1}} \quad \text{(S8-3)}$$

Table S 7: Fitting parameter for the decreasing intensity of the carbonyl band at 1908 cm^{-1} with radiation of 365 nm.

	1908 cm^{-1}
y_0	-0.0269 ± 0.0384
A_1	1.0327 ± 0.0371
t_1	115.3407 ± 11.2487

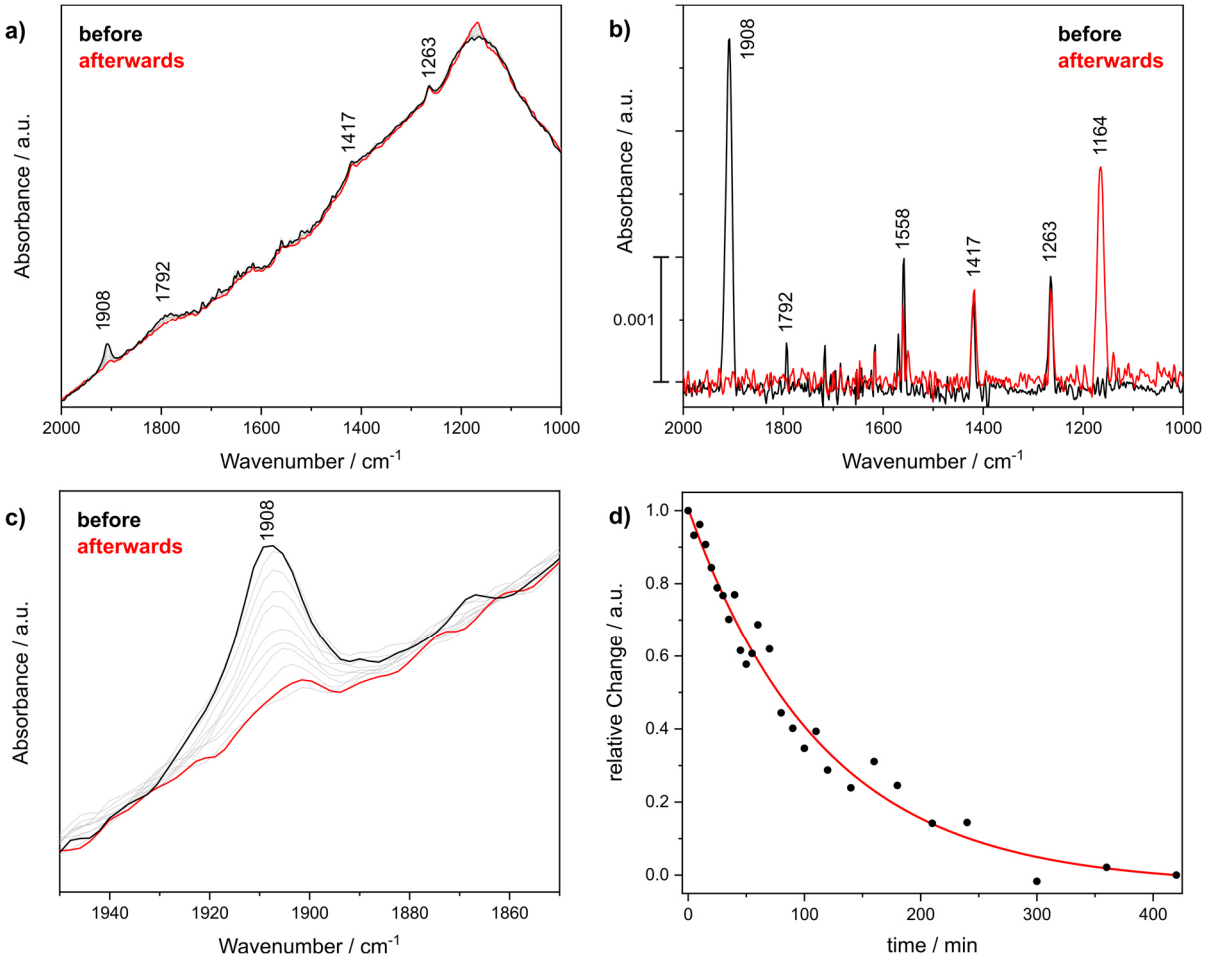

Figure S23: Spectra of the reactivity experiment of a monolayer (slightly thicker than a monolayer) of $[Mo(CO)_3(Py_3S_3)]$ (**1**) adsorbed on a Au(111) surface towards radiation with 465 nm under oxygen atmosphere: a) original spectra with the bessel function between 2000 cm^{-1} amd 1000 cm^{-1}; b) evaluated spectra without bessel function; c) enlargement of the symmetric CO stretching vibration; d) relative decrease of the absorption intensities at 1908 cm^{-1}; the PEM maximum efficiency was set for the half-wave (WAV) at 1750 cm^{-1}.

Figure S23 shows the IRRA spectra after reaction of the adsorbed complex **1** with oxygen under radition with 365 nm. After 420 min nearly no intensity of the symmetric carbonyl band of **1** is left. Furthermore, the spectra from before and afterwards have hardly changed. Only the band at 1164 cm^{-1} has been added. The typical ligand bands at 1558 cm^{-1}, 1417 cm^{-1} and 1263 cm^{-1} have not changed. Finally, it can be concluded from this experiment that the ligand has remained intact and that the carbonyl ligands have been displaced from the coordination sphere by photodissociation. For the latter reaction, a half-life $t_{1/2}$ of 77.8 min was determined. Compared to the azakalixpyridine system, the half-life is 10 times longer. This confirms the significantly lower reactivity of the complex $[Mo(CO)_3(Py_3S_3)]$ (**1**) compared to its azakalixpyridine analogue.

8.3 Calculation of the hypothetically molybdenum(VI) trioxo complex supported by the thiacalixpyridine ligand [$MoO_3(Py_3S_3)$] (3)

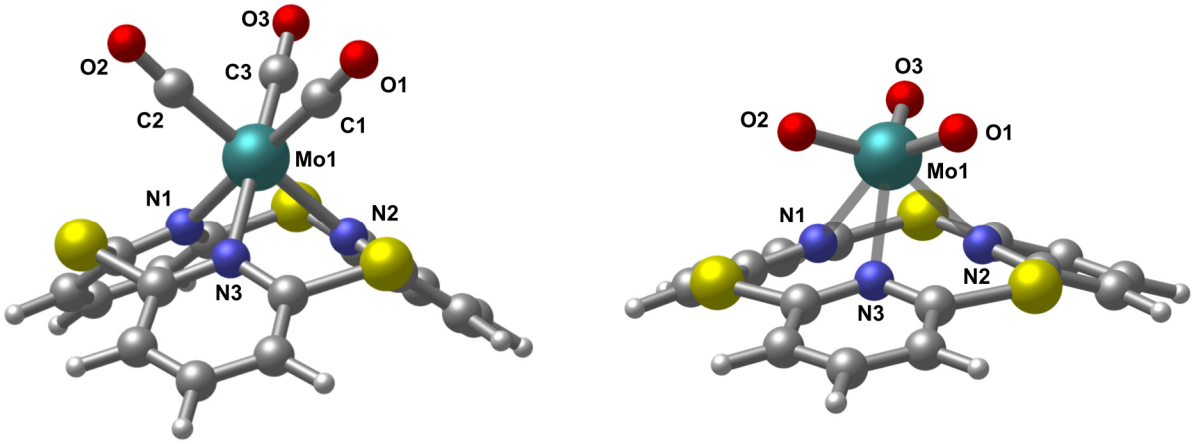

Figure S24: Shown are the calculated structures for [$Mo(CO)_3(Py_3S_3)$] (**1**) (left) and [$MoO_3(Py_3S_3)$] (**3**) (right).

Table S8: Comparison of the calculated bong length and angles of the complex [$Mo(CO)_3(Py_3S_3)$] (**1**) and the hypothetically trioxo complex [$MoO_3(Py_3S_3)$].

[$Mo(CO)_3(Py_3S_3)$] (1)				[$MoO_3(Py_3S_3)$] (3)			
Mo(1)-C(1)	1.949	N(1)-Mo(1)-C(3)	97.79	Mo(1)-O(1)	1.713	N(1)-Mo(1)-O(3)	87.34
Mo(1)-C(2)	1.950	N(2)-Mo(1)-C(1)	96.83	Mo(1)-O(2)	1.712	N(2)-Mo(1)-O(1)	86.58
Mo(1)-C(3)	1.949	N(2)-Mo(1)-C(3)	97.26	Mo(1)-O(3)	1.712	N(2)-Mo(1)-O(3)	85.66
Mo(1)-N(1)	2.252	N(3)-Mo(1)-C(1)	96.61	Mo(1)-N(1)	2.424	N(3)-Mo(1)-O(1)	87.40
Mo(1)-N(2)	2.252	N(3)-Mo(1)-C(2)	96.46	Mo(1)-N(2)	2.423	N(3)-Mo(1)-O(2)	85.62
Mo(1)-N(3)	2.246	C(1)-Mo(1)-C(2)	84.45	Mo(1)-N(3)	2.428	O(1)-Mo(1)-O(2)	108.28
O(1)-C(1)	1.155	C(1)-Mo(1)-C(3)	83.73			O(1)-Mo(1)-O(3)	108.05
O(2)-C(2)	1.155	C(2)-Mo(1)-C(3)	84.09			O(2)-Mo(1)-O(3)	108.01
O(3)-C(3)	1.155	N(1)-Mo(1)-N(2)	81.90			N(1)-Mo(1)-N(2)	73.05
		N(1)-Mo(1)-N(3)	82.01			N(1)-Mo(1)-N(3)	72.72
N(1)-Mo(1)-C(1)	178.12	N(2)-Mo(1)-N(3)	82.04	N(1)-Mo(1)-O(1)	153.66	N(2)-Mo(1)-N(3)	72.92
N(2)-Mo(1)-C(2)	178.22	Mo(1)-C(1)-O(1)	176.78	N(2)-Mo(1)-O(2)	154.57		
N(3)-Mo(1)-C(3)	179.29	Mo(1)-C(2)-O(2)	176.80	N(3)-Mo(1)-O(3)	154.05		
N(1)-Mo(1)-C(2)	96.79	Mo(1)-C(3)-O(3)	176.55	N(1)-Mo(1)-O(2)	85.99		

Table S9: Shown are the average Mayer bond orders for the molybdenum bonds of the calculated tricarbonyl and trioxo complexes supported by the thiacalixpyridine ligand **2** and the previously reported azacalixpyridine ligand.[17,22]

	[$Mo(CO)_3(Py_3S_3)$] (1)	[$MoO_3(Py_3S_3)$] (3)	[$Mo(CO)_3$(Tolyl-ACP)] [a]	[MoO_3(Tolyl-ACP)] [a]
Mo-N	0.7485	0.2671	0.3085	0.3068
Mo-C	1.4002	--------	1.3792	--------
Mo-O	--------	1.8036	--------	1.7448

[a] Values from Reference [17] and [22].

8 Reactivity towards oxygen (O_2)

Table S 10: Free Gibbs energy, enthalpy, single-point energy of the gas phase (E_{gas}) and in THF solution (E_{soln}), solvation energy (G_{solv}) and free Gibbs energy in solution for both molybdenum complexes $[Mo(CO)_3(Py_3S_3)]$ (**1**) and $[MoO_3(Py_3S_3)]$ (**3**) using the methodology described in computional details (see SI Chapter 1).

Molecule	**1**	**3**	**O_2**	**CO**
Free Gibbs energy [Ha]	-2344.723656	-2228.625826	-150.251938	-113.247022
Enthalpy [Ha]	-2344.647455	-2228.560195	-150.228686	-113.228864
E_{soln} [Ha]	-2343.166394	-2228.950308	-150.250511	-113.233007
E_{gas} [Ha]	-2343.129570	-2228.946534	-150.243118	-113.237267
ΔG_{solv} [Ha]	-0.036824	-0.003773	-0.007393	-0.004260
S = (calc. spin state)	0	0	1	0
G_{soln} [Ha]	-2344.760480	-2228.629599	-150.259331	-113.251282

9 Computational Details

9.1 Coordinates of DFT-calculated structures of [Mo(CO)$_3$(Py$_3$S$_3$)] (1)

Table S 11: Atomic coordinates of the DFT-calculated structure of [Mo(CO)$_3$(Py$_3$S$_3$)] (**1**)

	x	y	z		x	y	z
C	-1.14987	-1.28731	-1.94047	C	4.25558	-0.88651	0.29718
C	-1.87397	-0.90952	-0.82448	C	4.87236	-1.24209	1.48257
C	-1.26498	-0.11248	0.13276	H	4.64901	-1.19202	-0.66168
N	-0.00343	0.33641	0.02099	C	4.26137	-0.89402	2.67318
C	0.71712	-0.12528	-1.01434	C	3.10385	-0.13175	2.63547
C	0.18095	-0.91966	-2.01612	Mo	0.86570	1.79476	1.50208
H	0.81419	-1.24247	-2.82986	C	1.63817	3.01030	2.81692
S	-2.24896	0.39305	1.50277	C	1.63847	3.01893	0.19591
C	-1.25809	-0.12727	2.86204	C	-0.61492	3.06318	1.49688
N	0.00266	0.32368	2.97412	O	2.07648	3.77983	3.55930
S	2.39958	0.36090	-1.19632	O	-1.44602	3.86575	1.48341
C	3.09847	-0.12412	0.34518	O	2.07699	3.79381	-0.54081
N	2.55658	0.31537	1.49306	H	-1.57849	-1.94213	5.68992
S	2.40994	0.34236	4.18266	H	-2.88343	-1.25417	3.66446
C	0.72831	-0.14751	4.00169	H	5.78845	-1.81762	1.47852
C	-1.86088	-0.93773	3.81191	H	4.65946	-1.20552	3.62818
C	0.19836	-0.95534	4.99589	H	-1.60168	-1.89215	-2.71545
C	-1.13151	-1.32660	4.92060	H	-2.89692	-1.22473	-0.67700
H	0.83557	-1.28529	5.80363				

Table S 12: Atomic coordinates of the DFT-calculated structure of [MoO$_3$(Py$_3$S$_3$)]

	x	y	z		x	y	z
Mo	17.25681	3.79391	10.58577	H	21.88922	1.64861	9.12442
S	19.27609	1.69561	8.39202	C	22.25540	3.41667	10.30067
S	19.78551	6.36263	11.13331	H	23.29844	3.19285	10.48875
S	15.44431	5.53531	7.95887	C	21.70157	4.59774	10.75284
N	17.27718	3.53545	8.17133	H	22.29069	5.33717	11.27941
N	19.56648	3.96019	9.87158	C	20.35457	4.83524	10.50260
N	17.54297	6.00195	9.62788	C	18.37913	6.85883	10.22157
C	16.29744	4.09456	7.45474	C	18.18406	8.23665	10.21107
C	15.83341	3.55932	6.25799	H	18.88799	8.88335	10.71831
H	15.03085	4.05116	5.72441	C	17.09688	8.74396	9.52915
C	16.43459	2.41663	5.77037	H	16.91111	9.81101	9.50735
H	16.09411	1.96895	4.84457	C	16.28514	7.87807	8.82404
C	17.51370	1.88677	6.44804	H	15.46586	8.23589	8.21447
H	18.05934	1.03302	6.06828	C	16.55310	6.51534	8.88993
C	17.91106	2.48628	7.63880	O	15.57483	4.08952	10.46192
C	20.14088	2.87182	9.35178	O	17.80360	4.45342	12.06835
C	21.47869	2.55181	9.55632	O	17.50210	2.09955	10.63756

9.2 Calculation of the IRRA spectrum of [Mo(CO)$_3$(Py$_3$S$_3$)] (1)

A frequency calculation is required for the simulation of an IRRA spectrum. The calculation is performed as a single molecule calculation (gas phase). In the IRRA spectroscopy the orientation of the transition dipol moment (TDM) of a certain vibration is important due to the surface selection rule. Hereby, the vibrational modes with a component in z direction will be reinforced and the intensity of vibrational modes oriented in the xy plane are vanished.

The intensity of a vibrational mode (I_{sum}) is the sum of the components of the transition dipole moment along the three spatial axis x, y and z, as shown in equation 9.1. TDM_x symbolizes the component along the x-axis, TDM_y along the y-axis and TDM_z along the z-axis.

$$I_{sum} = TDM_X{}^2 + TDM_y{}^2 + TDM_z{}^2 \quad (9.1)$$

For the simulation of the IRRA spectrum, only the component along the z-axis is taken into account due to the surface selection rule of IRRA spectroscopy, see equation 9.2. Note, the metal surface lies in the xy plane and the surface normal n represents the z-axis.

$$I_{IRRAS} = TDM_z{}^2 \quad (9.2)$$

For a good fit between the calculated and the measured spectrum, the approximate adsorption geometry on the surface must be known. Before performing the frequency calculation, the molecule has to be oriented within the space in the same (or nearly the same) way as it adsorbs on the surface.

The correct adsorption geometry can be determined in three ways. (1) the geometry is already known by measuring with other methods (STM, AFM, NEXAFS); (2) interpretation of the measured IRRA spectrum by missing or attenuated absorption bands compared to the bulk IR spectrum; (3) guess the initial structure and then adjust it until it fits.

Due to the missing intensity of the two vibrational modes A'(2) and A'' of the CO ligands in the IRRA spectrum and by knowing that the transition dipole moments are orthogonal to each other (see above Chapter 4.2), the adsorption geometry of the investigated complex [Mo(CO)$_3$(Py$_3$S$_3$)] (**1**) could be derived. In this case, for the simulation of the IRRA spectrum of complex **1** the three nitrogen donor atoms are aligned parallel to the surface (in the xy plane).

Table S13 demonstrate, how we can simulated a IRRA spectrum. For a small selection of vibrational modes from the full vibrational anlaysis of Table S2 the values of the transition dipole moments along the three axis are shown. By squaring the TDM_z value, the intensity of the IRRA spectrum can be obtained. The vibrational modes 49 to 51 represent the absorption bands of the CO ligands. When the three nitrogen donor atoms are aligned in the xy plane, only one absorption band is observed in the simulated IRRA spectrum, which corresponds to the totally symmetric vibration A'(1) (mode 51). This result is in excellent agreement with the experimental data (see Figure 4).

Table S 13: Shown are the values for the calculated IR spectrum of [$Mo(CO)_3(Py_3S_3)$] (**1**). It contains the sum intensity I_{sum} of a vibrational modes, the components of the transition dipole moments (TDM) along the x-, y- and z-axis and the IRRAS intensity $I_{IRRAS.}$ (For demonstration, only the modes 43-51 from the full vibrational analysis (see Table S2) are shown here).

Mode	calc. freq. uncorr.	calc. freq. corr.	I_{sum}	TDM_x	TDM_y	TDM_z	I_{IRRAS}
43	1583.8	1520.1	0.00	0.00	0.01	-0.00	0.00
44	1596.7	1531.0	10.43	-3.22	-0.13	0.07	0.01
45	1597.5	1531.7	11.16	0.13	-3.33	0.00	0.00
46	1617.1	1548.2	0.77	-0.86	-0.04	0.16	0.03
47	1617.4	1548.6	1.12	-0.08	1.05	0.00	0.00
48	1626.0	1555.8	10.84	-0.14	0.03	-3.28	10.82
49	1960.9	1839.3	996.2	3.56	-31.36	0.11	0.01
50	1962.3	1840.4	986.8	-31.18	-3.78	0.18	0.04
51	2034.2	1901.3	2199.4	-0.14	-0.04	-46.89	2199.4

References

1 A. Pal, J. E. Debreczeni, M. Sevvana, T. Gruene, B. Kahle, A. Zeeck and G. M. Sheldrick, *Acta Cryst. Sect. A: Found Adv.*, 2008, **64**, 985–992.
2 G. M. Sheldrick, *Acta Crystallogr. Sec. C: Struct. Chem.*, 2015, **71**, 3–8.
3 F. Neese, *WIREs Comput. Mol. Sci.*, 2018, **8**, 33.
4 J. P. Perdew, K. Burke and M. Ernzerhof, *Phys. Rev. Lett.*, 1996, **77**, 3865–3868.
5 F. Weigend and R. Ahlrichs, *Phys. Chem. Chem. Phys.*, 2005, **7**, 3297–3305.
6 a) A. Schäfer, C. Huber and R. Ahlrichs, *J. Chem. Phys.*, 1994, **100**, 5829–5835; b) A. Schäfer, H. Horn and R. Ahlrichs, *J. Chem. Phys.*, 1992, **97**, 2571–2577.
7 a) S. Grimme, S. Ehrlich and L. Goerigk, *J. Comput. Chem.*, 2011, **32**, 1456–1465; b) S. Grimme, J. Antony, S. Ehrlich and H. Krieg, *J. Chem. Phys.*, 2010, **132**, 154104.
8 F. Neese, F. Wennmohs, A. Hansen and U. Becker, *Chem. Phys.*, 2009, **356**, 98–109.
9 F. Neese, *J. Comput. Chem.*, 2003, **24**, 1740–1747.
10 K. Eichkorn, F. Weigend, O. Treutler and R. Ahlrichs, *Theor. Chem. Acc.*, 1997, **97**, 119–124, https://doi.org/10.1007/s002140050244.
11 K. Eichkorn, O. Treutler, H. Öhm, M. Häser and R. Ahlrichs, *Chem. Phys. Lett.*, 1995, **240**, 283–290.
12 A. D. Becke, *The Journal of Chemical Physics*, 1993, **98**, 5648–5652.
13 A. V. Marenich, C. J. Cramer and D. G. Truhlar, *J. Phys. Chem. B*, 2009, **113**, 6378–6396.
14 B. D. Matson and J. C. Peters, *ACS Catal.*, 2018, **8**, 1448–1455.
15 A. Schlimm, N. Stucke, B. M. Flöser, T. Rusch, J. Krahmer, C. Näther, T. Strunskus, O. M. Magnussen and F. Tuczek, *Chem. Eur. J.*, 2018, **24**, 10732–10744.
16 F. Petersen, I. Lautenschläger, A. Schlimm, B. M. Flöser, H. Jacob, R. Amirbeigiarab, T. R. Rusch, T. Strunskus, O. Magnussen and F. Tuczek, *Dalton Trans.*, 2021, **50**, 1042–1052.
17 K. U. Clausen, A. Schlimm, K. Bedbur, C. Näther, T. Strunskus, L. Fu, M. Gruber, R. Berndt and F. Tuczek, *Chem. Eur. J.*, 2024, **30**, e202303912.
18 a) H. Jacob, S. Ulrich, U. Jung, S. Lemke, T. Rusch, C. Schütt, F. Petersen, T. Strunskus, O. Magnussen, R. Herges and F. Tuczek, *Phys. Chem. Chem. Phys.*, 2014, **16**, 22643–22650; b) A. Schlimm, R. Löw, T. Rusch, F. Röhricht, T. Strunskus, T. Tellkamp, F. Sönnichsen, U. Manthe, O. Magnussen, F. Tuczek and R. Herges, *Angew. Chem.*, 2019, **131**, 6646–6650; c) T. R. Rusch, A. Schlimm, N. R. Krekiehn, B. M. Flöser, F. Röhricht, M. Hammerich, I. Lautenschläger, T. Strunskus, R. Herges, F. Tuczek and O. M. Magnussen, *J. Phys. Chem. C*, 2019, **123**, 13720–13730.
19 a) A. Shaporenko, A. Terfort, M. Grunze and M. Zharnikov, *J. El. Spec. Rel. Phenom.*, 2006, **151**, 45–51; b) M. E. Fleet, S. L. Harmer, X. Liu and H. W. Nesbitt, *Surface Science*, 2005, **584**, 133–145; c) H. Jacob, K. Kathirvel, F. Petersen, T. Strunskus, A. Bannwarth, S. Meyer and F. Tuczek, *Langmuir*, 2013, **29**, 8534–8543; d) E. Fast, A. Schlimm, I. Lautenschläger, K. U. Clausen, T. Strunskus, C. Spormann, T. K. Lindhorst and F. Tuczek, *Chem. Eur. J.*, 2020, **26**, 485–501.
20 a) A. Nefedov and C. Wöll, in *Surface Science Techniques*, ed. G. Bracco and B. Holst, Springer Berlin Heidelberg, Berlin, Heidelberg, 2013, pp. 277–303; b) J. Stöhr and D. A. Outka, *Phys. Rev. B*, 1987, **36**, 7891–7905; c) J. Stöhr, *NEXAFS spectroscopy*, Springer Science & Business Media, 2013.
21 a) Y. Liu, P. Feng, Z. Wang, X. Jiao and F. Akhtar, *Sci. Rep.*, 2017, **7**, 1845; b) C.V. Subba Reddy, E. H. Walker, C. Wen and S.-i. Mho, *J. Power Sources*, 2008, **183**, 330–333.
22 K. U. Clausen, N. Pienack, J. Gripp and F. Tuczek, *Chem. Eur. J.*, 2024, **30**, e202304359.